High harmonic generation from electrons moving in topological spin textures

Atsushi Ono ,[1] Shun Okumura ,[2] Shohei Imai ,[3] and Yutaka Akagi [3]

[1]*Department of Physics, Tohoku University, Sendai 980-8578, Japan*
[2]*Department of Applied Physics, The University of Tokyo, Hongo, Tokyo 113-8656, Japan*
[3]*Department of Physics, Graduate School of Science, The University of Tokyo, 7-3-1 Hongo, Tokyo 113-0033, Japan*

High harmonic generation (HHG) is a striking phenomenon, which reflects the ultrafast dynamics of electrons. Recently, it has been demonstrated that HHG can be used to reconstruct not only the energy band structure but also the geometric structure characterized by the Berry curvature. Here, we numerically investigate HHG arising from electrons coupled with a topological spin texture in a spin scalar chiral state where time reversal symmetry is broken. In this system, a sign change in scalar chirality alters the sign of the Berry curvature while keeping the energy band structure unchanged, allowing us to discuss purely geometrical effects on HHG. Notably, we found that, when the optical frequency is significantly lower than the energy gap, the sign of scalar chirality largely affects the longitudinal response parallel to the optical field rather than the transverse response. Our analysis suggests that this can be attributed to interband currents induced by the recombination of electron-hole pairs whose real-space trajectories are modulated by the anomalous velocity term.

I. INTRODUCTION

With the advancement of laser technology, ultrafast phenomena in the subfemtosecond and attosecond domains are being actively researched [1–14]. High harmonic generation (HHG) and high-order sideband generation (HSG) are representative examples, and recent research has progressed in solids such as semiconductors [15–37], strongly correlated electron systems [38–59], and magnetic materials [60–69]. In HHG and HSG, high-order harmonics are literally generated, and the details of their spectra and chirping have been well captured by the three-step model [70–74]. According to this model, the elementary processes of HHG, for example, consist of (i) ionization of electrons to the vacuum or excitation to the conduction bands, (ii) acceleration, and (iii) recombination of the electrons or the electron-hole pairs. Therefore the electronic structure is embedded in the high harmonic spectrum, and using this property, all-optical reconstruction of energy bands through HHG and HSG has been proposed and experimentally demonstrated [74–79].

Recently, it has become increasingly clear that HHG can be used to extract not only the energy band structure but also the geometric structure of electrons, characterized by the Berry curvature or the Berry phase [80–90]. As is well known, the Berry curvature appears in systems where either spatial inversion symmetry or time reversal symmetry is broken. Hitherto, high harmonics dependent on the Berry curvature have been observed in systems with broken spatial inversion symmetry, for example, in a monolayer MoS_2 [80] and the surface states of a topological insulator Bi_2Te_3 [81]. Additionally, in a Weyl semimetal WP_2 [82], the Berry curvature has been successfully reconstructed in reciprocal space. However, studies on the effects of geometric structures in HHG have been scarce for systems with broken time reversal symmetry [91].

Systems exhibiting nonzero Berry curvature due to broken time reversal symmetry include those with what are called topological spin textures. For example, in skyrmion crystals, interesting perturbative linear responses such as the topological Hall effect [92] and the magneto-optical effect [93–97] have been reported and discussed. However, nonlinear responses, including HHG or HSG, have received limited attention [98,99], even though the magnetic structure is expected to be embedded in the high harmonic spectrum through the dynamics of electrons coupled with topological spin textures.

A spin scalar chiral state can be considered as one of the simplest topological spin textures. It features a four-sublattice magnetic order [Figs. 1(a) and 1(b)], where the Chern number of each energy band takes on an integer value, leading to the emergence of the anomalous (topological) Hall effect [100,101]. Hence, this state can be viewed as a skyrmion crystal state with the smallest magnetic unit cell. Last year, two groups experimentally reported that the scalar chiral state is realized in $CoTa_3S_6$ and $CoNb_3S_6$ [102–104], attracting significant interest. In this study, we numerically analyze HHG in the scalar chiral state. We found that the transverse response, as naively expected to reflect the Berry curvature, indeed appears. Furthermore, we discovered that the sign of the Berry curvature is reflected in the longitudinal response even in cases where it predominates over the transverse response. This finding differs from the effects of anomalous velocity in intraband currents that have been discussed previously. We argue that the anomalous velocity modulates the recombination conditions of electron-hole pairs, potentially changing the interband current spectrum, on the basis of an analysis of the real-space dynamics of electron-hole pairs.

The rest of this paper is organized as follows. In Sec. II, we introduce our model and methods, and in Sec. III, we present numerical results. Section III A provides an overview
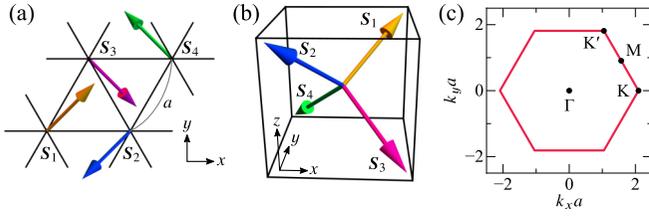
FIG. 1. (a) Magnetic unit cell of the four-sublattice spin scalar chiral state and (b) configuration of the four localized spin vectors, adapted from Ref. [105]. (c) Magnetic Brillouin zone.

of the equilibrium properties, focusing particularly on its geometric structure, and Sec. III B displays the high harmonic spectrum obtained from real-time evolution. The analysis of the real-space dynamics of electron-hole pairs is conducted in Sec. III C. Section III D discusses HHG for parameters close to those for $CoTa_3S_6$ and $CoNb_3S_6$. Sections IV and V are respectively devoted to the discussion and summary. Appendices A–D provide results for near-resonant and circular polarization driving, as well as comparisons with the 120° Néel state, where the Berry curvature is absent, and with perturbative responses.

II. MODEL AND METHOD

To examine the dynamics of electrons coupled with spin textures, we consider the ferromagnetic Kondo lattice model on a two-dimensional triangular lattice. The Hamiltonian is defined by

$$\mathcal{H} = \sum_{ijs} h_{ij} c_{is}^{\dagger} c_{js} - J_{\mathrm{K}} \sum_{iss'} \boldsymbol{S}_i \cdot \boldsymbol{\sigma}_{ss'} c_{is}^{\dagger} c_{is'}, \quad (1)$$

where $c_{is}^{\dagger}$ is a creation operator of an electron at site i with spin s, $\boldsymbol{\sigma}$ is a three-component vector of the Pauli matrices, and $\boldsymbol{S}_i$ is a classical vector describing a localized spin at site i. The transfer integral and the exchange interaction strength are denoted by h_{ij} and J_{K}, respectively. Considering that the electron dynamics induced by external fields occur on time scales of the order of subpicoseconds, we assume in this study that a magnetic order of $\{\boldsymbol{S}_i\}$ is not disturbed by electron motions; that is, each $\boldsymbol{S}_i$ is frozen during the real-time evolution of the electrons.

While the Hamiltonian in Eq. (1) is invariant under the global rotation of $\{\boldsymbol{S}_i\}$ and $\boldsymbol{\sigma}$, we explicitly define the four-sublattice scalar chiral state as

$$\boldsymbol{S}_1 = \frac{(1,1,1)}{\sqrt{3}}, \quad \boldsymbol{S}_2 = \frac{(-1,-1,1)}{\sqrt{3}},$$

$$\boldsymbol{S}_3 = \frac{(1,-1,-1)}{\sqrt{3}}, \quad \boldsymbol{S}_4 = \frac{(-1,1,-1)}{\sqrt{3}}, \quad (2)$$

where $\boldsymbol{S}_m$ represents the localized spin of sublattice m instead of site i (see Fig. 1). For this choice of $\{\boldsymbol{S}_m\}$, the scalar chirality, defined by

$$\chi = \boldsymbol{S}_1 \cdot (\boldsymbol{S}_2 \times \boldsymbol{S}_3) + \boldsymbol{S}_4 \cdot (\boldsymbol{S}_3 \times \boldsymbol{S}_2), \quad (3)$$

has a positive value of $\chi = 8/(3\sqrt{3}) \equiv \chi_0$. The sign of χ is changed by time reversal: $\boldsymbol{S}_m \mapsto -\boldsymbol{S}_m$ for all m; this operation is equivalent to $J_{\mathrm{K}} \mapsto -J_{\mathrm{K}}$ in the electron system, while the

band structure remains unchanged, since the localized spins $\boldsymbol{S}_m$ are treated classically.

Assuming sublattice structure, we can express the Hamiltonian in reciprocal space as

$$\mathcal{H} = \sum_{\boldsymbol{k}} \sum_{ss'} \sum_{mm'} h_{sm,s'm'}(\boldsymbol{k}) c_{\boldsymbol{k}sm}^{\dagger} c_{\boldsymbol{k}s'm'}, \quad (4)$$

where $\boldsymbol{k}$ denotes momentum, and the indices s and m correspond respectively to the spin and sublattice degrees of freedom. In the four-sublattice scalar chiral state, each energy band is doubly degenerated in the whole magnetic Brillouin zone (BZ) [Fig. 1(c)], and $h(\boldsymbol{k})$ is an 8×8 matrix that can be block diagonalized by the unitary transformation:

$$U^{\dagger} h(\boldsymbol{k}) U = h_+(\boldsymbol{k}) \oplus h_-(\boldsymbol{k}), \quad (5)$$

into two 4×4 matrices h_+ and h_-. Adopting $\{\boldsymbol{S}_m\}$ in Eq. (2), we can choose the unitary matrix U as

$$U = (\text{spin}) \otimes (\text{sublattice})$$

$$= \frac{1}{\sqrt{2}} \begin{bmatrix} -i & 0 & 0 & 0 & i & 0 & 0 & 0 \\ 0 & -i & 0 & 0 & 0 & i & 0 & 0 \\ 0 & 0 & -i & 0 & 0 & 0 & i & 0 \\ 0 & 0 & 0 & -i & 0 & 0 & 0 & i \\ 0 & 0 & 0 & 1 & 0 & 0 & 0 & 1 \\ 0 & 0 & 1 & 0 & 0 & 0 & 1 & 0 \\ 0 & 1 & 0 & 0 & 0 & 1 & 0 & 0 \\ 1 & 0 & 0 & 0 & 1 & 0 & 0 & 0 \end{bmatrix}, \quad (6)$$

which diagonalizes another unitary matrix V that commutes with $h(\boldsymbol{k})$. The latter unitary matrix,

$$V = \sigma_y \otimes \begin{bmatrix} 0 & 0 & 0 & 1 \\ 0 & 0 & 1 & 0 \\ 0 & 1 & 0 & 0 \\ 1 & 0 & 0 & 0 \end{bmatrix}, \quad (7)$$

represents a mirror reflection of electron spins with respect to the zx plane and a permutation of sublattice spins: $\boldsymbol{S}_1 \leftrightarrow \boldsymbol{S}_4$ and $\boldsymbol{S}_2 \leftrightarrow \boldsymbol{S}_3$, and it is diagonalized as

$$U^{\dagger} V U = \mathrm{diag}(+1,+1,+1,+1,-1,-1,-1,-1). \quad (8)$$

The explicit form of $h_{\pm}$ is given by

$$h_{\pm}(\boldsymbol{k}) = -\frac{J_{\mathrm{K}}}{\sqrt{3}} \sigma_z \otimes \sigma_0 \pm \frac{J_{\mathrm{K}}}{\sqrt{3}} (\sigma_x + \sigma_y) \otimes \sigma_y$$

$$- 2h_1 \cos(k_x) \sigma_0 \otimes \sigma_x$$

$$- 2h_1 \cos\left(\frac{k_x + \sqrt{3}k_y}{2}\right) \sigma_x \otimes \sigma_0$$

$$- 2h_1 \cos\left(\frac{k_x - \sqrt{3}k_y}{2}\right) \sigma_x \otimes \sigma_x, \quad (9)$$

where σ_0 denotes the identity matrix. Here and throughout the paper, we consider only the transfer integral between the nearest neighbor sites, $h_{ij} = -h_1$. Given the above, we can write the Hamiltonian in Eq. (1) as

$$\mathcal{H} = \sum_{\boldsymbol{k}} \sum_{n=1}^{4} [\varepsilon_n^+(\boldsymbol{k}) a_{\boldsymbol{k}n}^{\dagger} a_{\boldsymbol{k}n} + \varepsilon_n^-(\boldsymbol{k}) b_{\boldsymbol{k}n}^{\dagger} b_{\boldsymbol{k}n}] \quad (10)$$

with $\varepsilon_n^+(\boldsymbol{k}) = \varepsilon_n^-(\boldsymbol{k}) \equiv \varepsilon_n(\boldsymbol{k})$. Here, $\varepsilon_n^\pm(\boldsymbol{k})$ is the nth eigen-energy of $h_\pm(\boldsymbol{k})$, and $a_{\boldsymbol{k}n}^\dagger$ and $b_{\boldsymbol{k}n}^\dagger$ are creation operators of electrons associated with $c_{\boldsymbol{k}sm}^\dagger$ through a unitary transformation. The block diagonal form of $h(\boldsymbol{k})$ in Eq. (5) facilitates the efficient computation of real-time dynamics and enables the calculation of the Berry curvature $\boldsymbol{B}_n = (0, 0, B_n)$ through the following formula:

$$B_n(\boldsymbol{k}) = \sum_{m(\neq n)} \frac{\langle \boldsymbol{k}n | v_x(\boldsymbol{k}) | \boldsymbol{k}m \rangle \langle \boldsymbol{k}m | v_y(\boldsymbol{k}) | \boldsymbol{k}n \rangle - \text{c.c.}}{[\varepsilon_n(\boldsymbol{k}) - \varepsilon_m(\boldsymbol{k})]^2} \quad (11)$$

with $\boldsymbol{v}(\boldsymbol{k}) = \partial_{\boldsymbol{k}} h_+(\boldsymbol{k})$ $[= \partial_{\boldsymbol{k}} h_-(\boldsymbol{k})]$, where $|\boldsymbol{k}n\rangle$ is an energy eigenstate satisfying $h_+(\boldsymbol{k})|\boldsymbol{k}n\rangle = \varepsilon_n(\boldsymbol{k})|\boldsymbol{k}n\rangle$. Note that $B_n(\boldsymbol{k})$ remains unchanged even if we adopt the eigenstates of $h_-(\boldsymbol{k})$, and the Chern number of the doubly degenerated nth band is given by

$$C_n = \int_{\text{BZ}} \frac{d^2k}{2\pi} 2B_n(\boldsymbol{k}), \quad (12)$$

where BZ stands for the magnetic BZ depicted in Fig. 1(c). We also introduce the linear optical conductivity [106],

$$\sigma_{\alpha\beta}(\omega) = \frac{\mathrm{i}T_{\alpha\beta} - \mathrm{i}\chi_{\alpha\beta}(\omega + \mathrm{i}\eta)}{\omega + \mathrm{i}\eta}, \quad (13)$$

with η being a positive infinitesimal, where

$$T_{\alpha\beta} = \int_{\text{BZ}} \frac{d^2k}{(2\pi)^2} \text{Tr}\big[\rho_{\boldsymbol{k}} \partial_{k_\alpha} \partial_{k_\beta} h(\boldsymbol{k})\big], \quad (14)$$

$$\chi_{\alpha\beta}(z) = 2\int_{\text{BZ}} \frac{d^2k}{(2\pi)^2} \sum_{mn} \frac{f_n(\boldsymbol{k}) - f_m(\boldsymbol{k})}{\varepsilon_m(\boldsymbol{k}) - \varepsilon_n(\boldsymbol{k}) - z}$$
$$\times \langle \boldsymbol{k}n | v_\alpha(\boldsymbol{k}) | \boldsymbol{k}m \rangle \langle \boldsymbol{k}m | v_\beta(\boldsymbol{k}) | \boldsymbol{k}n \rangle. \quad (15)$$

Here, $\rho_{\boldsymbol{k},mn} = \langle c_{\boldsymbol{k}n}^\dagger c_{\boldsymbol{k}m} \rangle$ represents a one-body density matrix of electrons, $f_n(\boldsymbol{k}) = \langle a_{\boldsymbol{k}n}^\dagger a_{\boldsymbol{k}n} \rangle = \langle b_{\boldsymbol{k}n}^\dagger b_{\boldsymbol{k}n} \rangle$ is the Fermi distribution function for the nth band, and $T_{\alpha\beta}$ in Eq. (14) is called a stress tensor. The prefactor 2 in Eq. (15) counts the equal contribution from the eigenstates of h_-.

The real-time dynamics are governed by the von Neumann equation with a phenomenological relaxation term,

$$\frac{d\rho_{\boldsymbol{k}}}{dt} = -\mathrm{i}[h(\boldsymbol{k}), \rho_{\boldsymbol{k}}] - \Gamma(\rho_{\boldsymbol{k}} - \rho_{0,\boldsymbol{k}}), \quad (16)$$

with t representing time. Here, $\rho_{0,\boldsymbol{k}}$ denotes the one-body density matrix in the ground state for a given $\boldsymbol{k}$, and Γ represents the relaxation rate. We assume that the initial state is the ground state, that is, $\rho_{\boldsymbol{k}}(-\infty) = \rho_{0,\boldsymbol{k}}$. Given our focus on the dynamics of electrons driven by optical fields, we consider only the coupling between the electric field and the electrons. The vector potential $\boldsymbol{A}(t)$ is introduced through the Peierls substitution: $\boldsymbol{k}(t) = \boldsymbol{k} - \boldsymbol{A}(t)$, and the electric field $\boldsymbol{F}$ is determined by $\boldsymbol{F}(t) = -\partial_t \boldsymbol{A}(t)$. In this study, we apply a continuous wave described by the following vector potential:

$$A_\alpha(t) = -\frac{F_{0,\alpha}}{\Omega} \sin(\Omega t - \phi_\alpha) \times \begin{cases} \mathrm{e}^{-t^2/(2\tau^2)} & (t < 0) \\ 1 & (t \geqslant 0) \end{cases} \quad (17)$$

for $\alpha = x, y$, where $\boldsymbol{F}_0 = (F_{0,x}, F_{0,y})$, Ω, ϕ_α, and τ represent the electric field amplitude, frequency, phase, and ramp time, respectively. Linear polarization is characterized by

$$F_{0,x} = F_0 \cos\psi, \quad F_{0,y} = F_0 \sin\psi, \quad \phi_x = \phi_y = \phi, \quad (18)$$

where ψ denotes the polarization angle measured from the x axis [see also Fig. 1(a)]. On the other hand, left/right circular polarization (LCP/RCP) is described by

$$F_{0,x} = F_{0,y} = F_0, \quad (\phi_x, \phi_y) = \begin{cases} (-\pi/2, 0) & \text{(LCP)} \\ (+\pi/2, 0) & \text{(RCP)} \end{cases}. \quad (19)$$

The electric current density $\boldsymbol{J}(t)$ is defined by

$$\boldsymbol{J}(t) = \frac{1}{N\mathcal{A}} \sum_{\boldsymbol{k}} \text{Tr}[\rho_{\boldsymbol{k}} \boldsymbol{v}(\boldsymbol{k})], \quad (20)$$

where N stands for the number of $\boldsymbol{k}$-points. The area of the magnetic unit cell is denoted by $\mathcal{A}$, and in the presence of four-sublattice orders, $\mathcal{A} = 2\sqrt{3}a^2$ with a being the lattice constant. The intensity of electromagnetic radiation is proportional to

$$I(\omega) = I_x(\omega) + I_y(\omega), \quad I_\alpha(\omega) = \omega^2 |J_\alpha(\omega)|^2 \quad (21)$$

for $\alpha = x, y$, where $\boldsymbol{J}(\omega)$ is the Fourier transformation of $\boldsymbol{J}(t)$.

The von Neumann equation (16) is numerically solved using the fourth-order Runge–Kutta method with a time step of $\delta t = 0.01\hbar/h_1$. The number of $\boldsymbol{k}$ points is set to $N = 50^2$ unless otherwise specified, for which we confirmed the convergence. In this paper, the nearest neighbor transfer integral h_1, the Dirac constant $\hbar$, the electric charge e, and the lattice constant a are set to one. Energy, time, electric current density, and electric fields are expressed in units of h_1, $\hbar/h_1$, $eh_1/(\hbar a)$, and $h_1/(ea)$, respectively. For $h_1 = 1$ eV and $a = 1$ nm, these read $\hbar/h_1 = 0.66$ fs, $eh_1/(\hbar a) = 2.4$ kA cm^{-1}, and $h_1/(ea) = 10$ MV cm^{-1}.

III. RESULTS

In this section, we give an overview of the equilibrium properties of the four-sublattice scalar chiral state. Then, we show the numerical results of the HHG when linearly polarized light is applied, and discuss how geometrical effects manifest themselves. Hereafter, we focus mainly on cases where the Kondo coupling is $J_K = 3$, and the electron number density is $n_e = 0.5$ (half filling) [107]. At half filling, the optical gap increases proportionally with J_K, which enables numerical analysis at optical frequencies that are sufficiently small relative to the gap, suppressing the excited electron density in the conduction bands. Additionally, despite the absence of the dc Hall effect at $n_e = 0.5$, optical transverse responses due to the nonzero Berry curvature can be observed, as shown in the following sections.

A. Equilibrium properties

Figure 2(a) displays the energy band structure $\varepsilon_n(\boldsymbol{k})$ in the magnetic BZ alongside the dc Hall conductivity as a function of the chemical potential. We observe four doubly degenerated bands in the magnetic BZ. The dc Hall conductivity $\sigma_{xy}(\omega = 0)$ exhibits a quantized value of $\pm e^2/(2\pi\hbar)$ when the electrons are at quarter or three quarter filling, as initially pointed out in Refs. [100,101]. Since time reversal symmetry is broken while spatial inversion symmetry is preserved, the Berry curvature satisfying $B_n(-\boldsymbol{k}) = B_n(\boldsymbol{k})$ can appear in the scalar chiral state. In Figs. 2(b) and 2(c), we present the Berry curvature $B_n(\boldsymbol{k})$ on the energy-band surfaces for $\chi = +\chi_0$ and
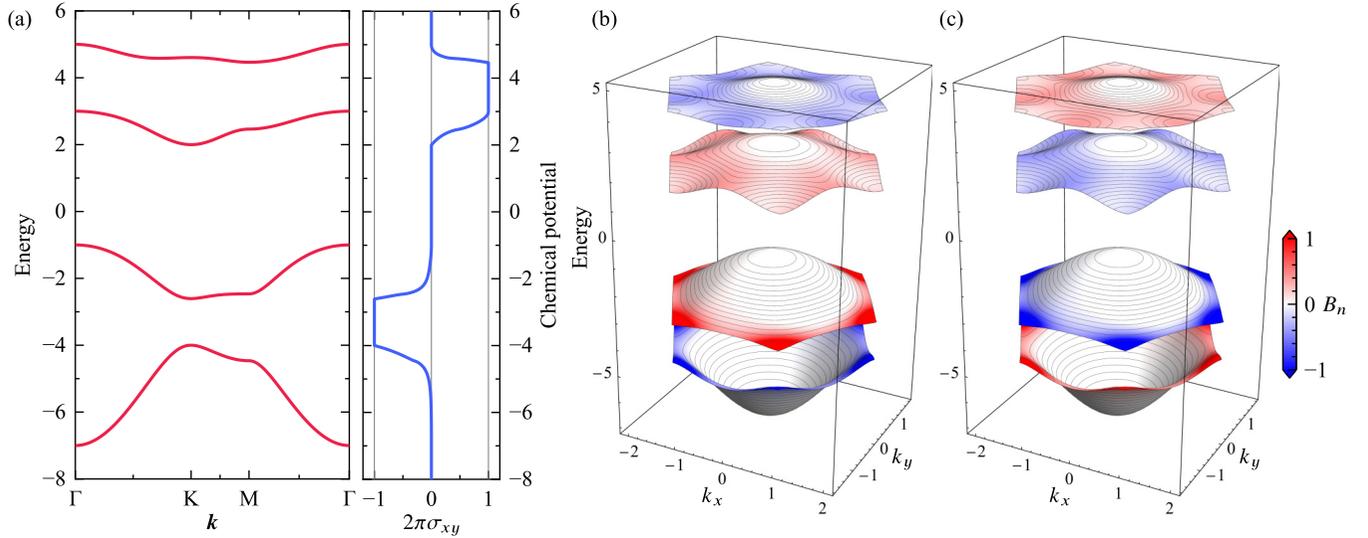
FIG. 2. (a) Energy band structure $\varepsilon_n(\mathbf{k})$ (left), and the chemical potential dependence of dc Hall conductivity $2\pi\sigma_{xy}(0)$ at zero temperature (right), in the four-sublattice scalar chiral state. The conductivity is calculated using Eqs. (13)–(15) with $\eta = 0.01$. [(b) and (c)] Berry curvature $B_n(\mathbf{k})$ plotted on the energy-band surfaces for (b) $\chi = +\chi_0$ and (c) $\chi = -\chi_0$.

$\chi = -\chi_0$. For the lower two doubly degenerated bands, the Berry curvature takes on large values at and in the vicinity of the K point, while for the upper two bands, the Berry curvature appears more dispersed throughout the BZ. Notably, the sign of the Berry curvature is reversed by changing the sign of χ without affecting the energy bands $\varepsilon_n(\mathbf{k})$. The Chern number defined in Eq. (12) is numerically confirmed to be $C_1 = -1$, $C_2 = +1$, $C_3 = +1$, and $C_4 = -1$ from the bottom to the top band when $\chi = +\chi_0$, and their signs are reversed for $\chi = -\chi_0$, as is consistent with the chemical potential dependence of the dc Hall conductivity. It should be emphasized that since the sign of scalar chirality alters only the sign of the Berry curvature, if the high harmonic spectrum differs depending on the chirality's sign, such a difference should be attributed not to the energy bands $\varepsilon_n(\mathbf{k})$ but to a purely geometrical effect originating from the Berry curvatures $\mathbf{B}_n(\mathbf{k})$.

In the case of $J_K = 3$ and $n_e = 0.5$, the longitudinal component of the optical conductivity, $\sigma_{xx}(\omega)$, and the transverse component, $\sigma_{xy}(\omega)$, are shown in Fig. 3. Although the direct
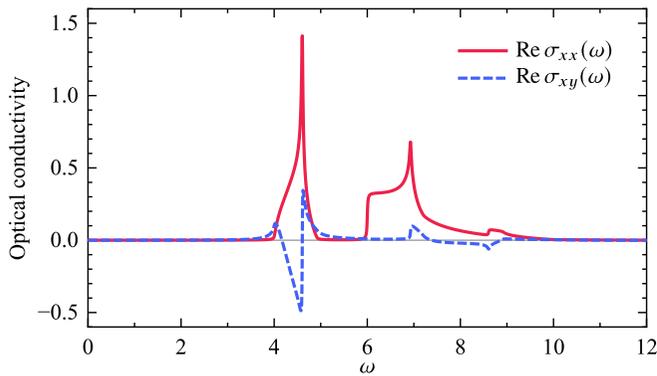
FIG. 3. Real part of optical conductivity in the scalar chiral state with $\chi = +\chi_0$ at zero temperature. The parameters are set to $J_K = 3$, $n_e = 0.5$, and $\eta = 0.01$.

optical band gap of $\varepsilon_3(\mathbf{k}) - \varepsilon_2(\mathbf{k}) = 4$ is at the Γ point, there, the transition dipole moment proportional to $\mathbf{v}(\mathbf{k})$ is zero; a significant absorption peak can be seen in $\sigma_{xx}(\omega)$ at $\omega = 4.6$, corresponding to the interband transition at the K point. At half filling, since the sum of the Chern numbers of the occupied bands is zero, the transverse conductivity $\sigma_{xy}(\omega)$ vanishes at $\omega = 0$, indicating no dc Hall effect. Nonetheless, for $\omega \gtrsim 4$, nonzero $\sigma_{xy}(\omega)$ arises owing to interband transitions, and the sign of $\sigma_{xy}(\omega)$ also depends on the sign of scalar chirality. This can be observed through linear magneto-optical effects, as discussed in Ref. [95]. Even beyond such a linear and perturbative regime, given that the electromagnetic radiation intensity is determined by the expectation value of a one-body electric current operator, we anticipate transverse HHG dependent on scalar chirality.

B. Real-time dynamics and HHG

In this section, we examine the real-time dynamics when a continuous wave [Eq. (17)] is applied, and discuss the characteristics of the resulting high harmonic spectrum. First, we consider the case where linearly polarized light parallel to the x axis (i.e., $\psi = 0$) is irradiated. The relaxation rate and the optical frequency are set to $\Gamma = 0.1$ and $\Omega = 10 \times 2\pi/500 = 0.126$, respectively, with the latter being sufficiently smaller than the optical gap. The ramp time in Eq. (17) and the phase in Eq. (18) are chosen as $\tau = 6$ and $\phi = 0$, respectively, which do not affect the high harmonic spectrum in a steady state.

We show the temporal profiles of the applied vector potential $\mathbf{A}(t) = (A_x(t), 0)$ and the electric current density $\mathbf{J}(t) = (J_x(t), J_y(t))$ in Figs. 4(a) and 4(b), respectively, when the electric field amplitude is $F_0 = 1$. Given the optical period of $T = 2\pi/\Omega = 50$, the system quickly reaches a steady state after a few optical cycles (on a time scale of the order of $\Gamma^{-1} = 10$), where not only the longitudinal current J_x but also the transverse current J_y is induced by the vector potential
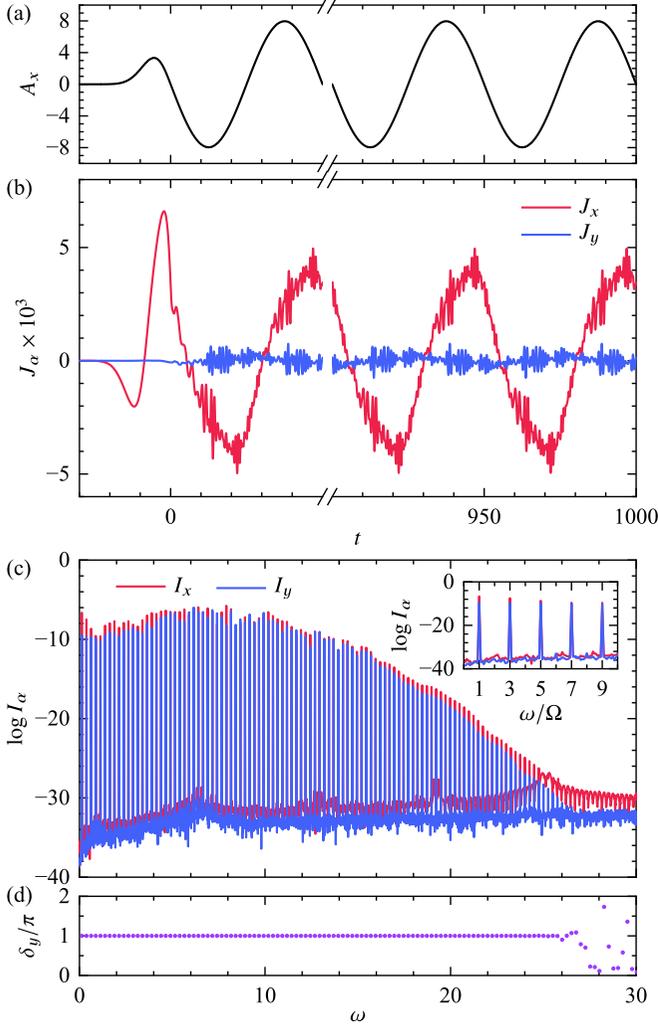
FIG. 4. [(a) and (b)] Temporal profiles of (a) the vector potential, $A_x(t)$, and (b) the electric currents, $J_x(t)$ and $J_y(t)$. (c) Power spectra of the electric currents, $I_x(\omega)$ and $I_y(\omega)$. The inset shows the intensity of low-order harmonics. (d) Phase difference in the transverse current $J_y(\omega)$ between states with opposite chiralities, $\delta_y = \arg J_y(\omega)|_{\chi=-\chi_0} - \arg J_y(\omega)|_{\chi=+\chi_0}$, for odd-order harmonics. The electric field amplitude, frequency, polarization angle, and ramp time are set to $F_0 = 1$, $\Omega = 0.126$, $\psi = 0$, and $\tau = 6$, respectively.

parallel to the x axis. Although J_y is less intense than J_x, its high-frequency oscillatory components are of similar magnitude to those of J_x. As becomes clear from the subsequent discussion related to Fig. 4(d), this transverse response is due to σ_{xy} ($\neq 0$) arising from scalar chirality, and as shown in Appendix C, it does not occur in the 120° Néel state when linear polarization is along a high symmetric direction such as $\psi = 0$ and $\pi/6$.

High harmonic spectrum $I(\omega)$ can be obtained using the Fourier transformation of $\mathbf{J}(t)$. In this study, we extracted real-time data for $500 < t \leqslant 1000$, considering the system to have reached the steady state before $t = 500$, and applied the fast Fourier transformation (FFT) to $(1000 - 500)/\delta t$ data points. The optical frequency of $\Omega = 10 \times 2\pi/500$ is consistent with this number of data points, so that the FFT results include data points at frequencies that are exact multiples of Ω.

Figure 4(c) displays the intensities of the longitudinal and the transverse response, $I_x(\omega)$ and $I_y(\omega)$, respectively, obtained from $J_x(t)$ and $J_y(t)$ shown in Fig. 4(b). Since the optical frequency is $\Omega = 0.126$, which is less than $1/30$ of the optical gap, the high harmonic spectrum up to approximately the 200th order is observed to be clearly separated from a background of $\lesssim 10^{-32}$. Furthermore, as the optical period and the number of data points used for FFT are consistent, sharp peaks appear only at frequencies that are integer multiples of Ω as shown in the inset of Fig. 4(c). These high harmonic peaks are observed at odd orders, while the even-order harmonics disappear because of the presence of spatial inversion symmetry. Overall, although the intensity of the transverse component, I_y, is several orders of magnitude lower than that of the longitudinal component, I_x, they appear in the same frequency range. Up to about $\omega \lesssim 10$, a plateau appears in the spectrum, which roughly agrees with the frequency range where the optical conductivity is nonzero (see Fig. 3); this is a characteristic widely observed in the HHG in the nonperturbative regime.

Here, we discuss how the transverse response J_y changes with respect to the sign of scalar chirality. We confirmed that, for $\chi = -\chi_0$, the power spectrum $I_y(\omega)$ is exactly the same as in the case of $\chi = +\chi_0$ shown in Fig. 4(c) [108]. However, a difference is observed in the phase spectrum. Figure 4(d) shows the difference in the phase component of $J_y(\omega)$, defined by $\delta_y = \arg J_y(\omega)|_{\chi=-\chi_0} - \arg J_y(\omega)|_{\chi=+\chi_0}$, for odd-order harmonics between the cases of $\chi = +\chi_0$ and $\chi = -\chi_0$. As clearly seen in Fig. 4(d), the transverse component of the odd-order harmonics differs in phases by π from each other. This indicates that the sign of the transverse response in the scalar chiral state is inverted by time reversal, implying its association with the presence of scalar chirality, or the Berry curvature.

We show in Fig. 5 the amplitude dependence of the high harmonic spectrum for $\chi = +\chi_0$. Figure 5(a) is a color map displaying the intensity of odd-order harmonics, $I(n\Omega)$, as a function of the electric field amplitude F_0. Corresponding to the plateau region observed in Fig. 4(c), the intensity in the region of $\omega \lesssim 10$ is enhanced for $F_0 \gtrsim 1$. The white dashed line in the figure indicates the upper bound of the Bloch oscillation frequency, which is $\omega = F_0$ in the case of $\psi = 0$. The frequency domain mainly below this line can include contributions from intraband currents.

The detailed amplitude dependence of the low-order harmonics is plotted in Fig. 5(b). For $F_0 \lesssim 0.1$, the Fourier amplitude of the nth harmonic, $J_x(n\Omega)$, is proportional to the nth power of F_0, indicating that HHG is in the perturbative regime. As F_0 increases, the higher-order harmonics begin to deviate from the perturbative regime, transitioning to the nonperturbative regime around $F_0 \sim 1$. The inset of the figure plots the fundamental harmonic amplitude $|J_x(\Omega)|$ on a linear scale. This is well fitted by the exponential function $\exp(-F_{\mathrm{th}}/F_0)$ with $F_{\mathrm{th}} = 13.22$ indicated by the black dashed line, and the excited electron density exhibits similar behavior (not shown), suggesting that interband tunneling excitation dominates for $F_0 \gtrsim 1.5$. Therefore, for $F_0 \lesssim 1.5$, tunneling excitation hardly occurs, and the geometrical effects on the tunneling probability discussed in Refs. [109,110] can be considered negligible.
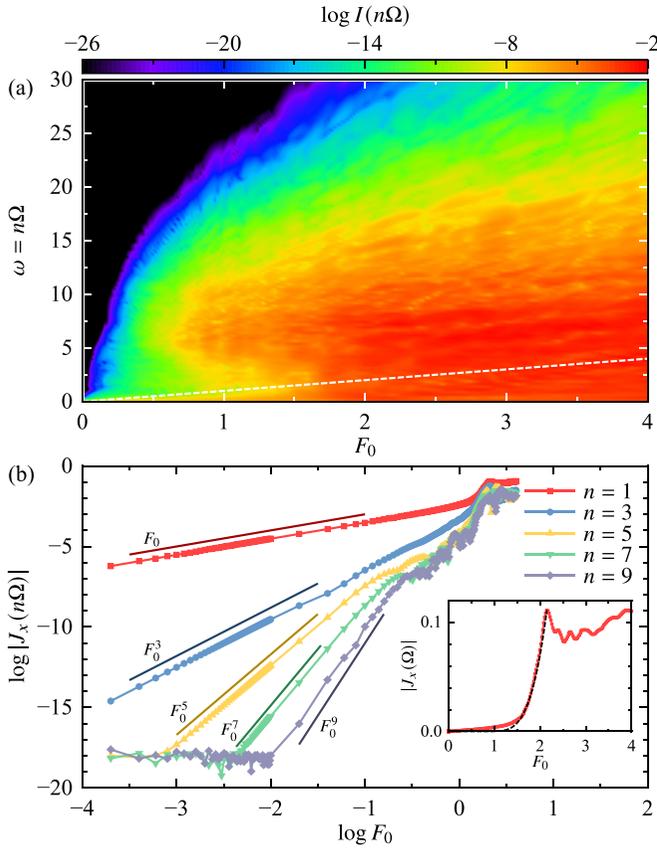
FIG. 5. (a) Amplitude dependence of the power spectrum of odd-order harmonics, $I(n\Omega)$ ($n = 1, 3, \dots$). The dashed line indicates the upper bound of the Bloch oscillation frequency (see main text). (b) Fourier amplitude of low-order harmonics, $J_x(n\Omega)$, as a function of F_0. The inset shows $J_x(\Omega)$ on a linear scale, with the dashed curve representing a fitted function, $|J_x(\Omega)| = 52.02 \exp(-13.22/F_0)$. The optical frequency and polarization angle are respectively set to $\Omega = 0.126$ and $\psi = 0$ in (a) and (b).

We examine the polarization angle ψ dependence of the nth harmonic intensity for $F_0 = 1$, as shown in Fig. 6. The red and blue lines correspond to the cases of $\chi = +\chi_0$ and $\chi = -\chi_0$, respectively. For the first-order harmonic, the difference due to the chirality sign is almost negligible, and it
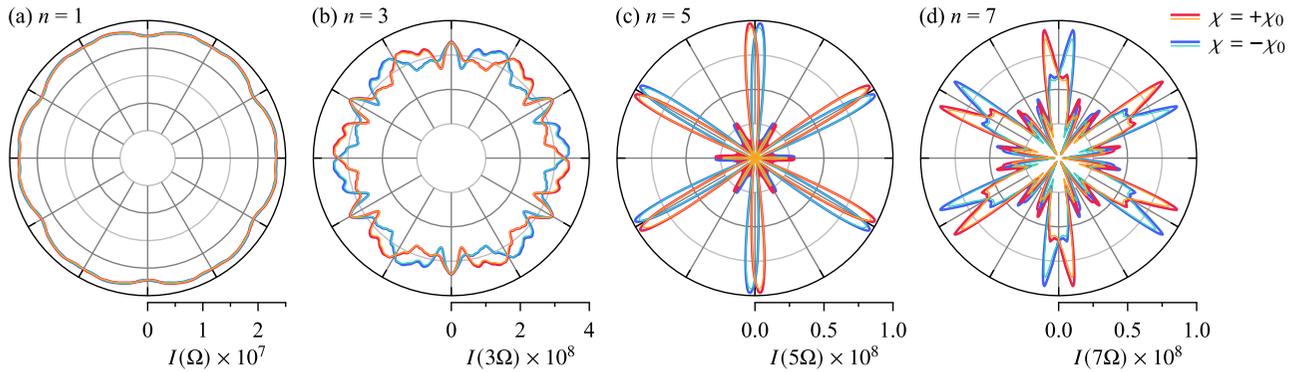
is approximately independent of the polarization angle. This partially inherits the property that, in the current system with sixfold symmetry, a linear optical response exhibits continuous rotational symmetry (see Appendix D for details). On the other hand, for the third and higher harmonics, not only does a significant dependence on the incident polarization angle appear, but clear differences are observed depending on the sign of scalar chirality. As previously mentioned, the chirality sign only changes the sign of the Berry curvature and does not alter the energy band structure; hence, this chirality dependence is attributed to purely geometrical effects.

The polarization angle dependence reflecting the sign of scalar chirality is naively expected to arise from the anomalous velocity of intraband currents, as discussed in the literature [80–86] for systems where spatial inversion symmetry is broken. The intraband current carried by an electron with momentum $\boldsymbol{k}$ in the nth band is proportional to

$$\dot{\boldsymbol{r}}_n = \partial_{\boldsymbol{k}} \varepsilon_n(\boldsymbol{k}) + \boldsymbol{F}(t) \times \boldsymbol{B}_n(\boldsymbol{k}), \quad (22)$$

where $\boldsymbol{r}$ is the position of the electron, and the second term is called the anomalous velocity. Note that the anomalous velocity term always produces a current perpendicular to the electric field $\boldsymbol{F}$. Therefore, to extract the contribution of the transverse response, the power spectrum $I(\omega)$ is decomposed into components parallel and perpendicular to $\boldsymbol{F}$, denoted by $I_\parallel(\omega)$ and $I_\perp(\omega)$, respectively. These are related to $I_x(\omega)$ and $I_y(\omega)$ through the relations:

$$I_\parallel = I_x \cos^2 \psi + 2\sqrt{I_x I_y} \cos \psi \sin \psi \cos \delta + I_y \sin^2 \psi, \quad (23)$$

$$I_\perp = I_x \sin^2 \psi - 2\sqrt{I_x I_y} \cos \psi \sin \psi \cos \delta + I_y \cos^2 \psi, \quad (24)$$

with $\delta(\omega) = \arg J_y(\omega) - \arg J_x(\omega)$. The thin curves in Fig. 6 show the polarization angle dependence of the intensity of the parallel component $I_\parallel(\omega) = I(\omega) - I_\perp(\omega)$. Contrary to expectation, for any ψ, we observe that $I_\parallel \approx I$, indicating that the anomalous velocity [and a component of $\partial_{\boldsymbol{k}} \varepsilon_n(\boldsymbol{k})$ that is perpendicular to $\boldsymbol{k}(t) = \boldsymbol{k} - \boldsymbol{A}(t)$] in the intraband current cannot explain the observed dependence on the sign of scalar chirality. Thus, in the following section, we consider interband currents associated with the recombination of electron-hole pairs.

FIG. 6. [(a)–(d)] Polarization angle dependence of the nth harmonic intensity $I(n\Omega)$ for $\chi = +\chi_0$ (red) and $\chi = -\chi_0$ (blue). The thin curves show the longitudinal component $I_\parallel(n\Omega)$ for $\chi = +\chi_0$ (orange) and $\chi = -\chi_0$ (cyan). The electric field amplitude and frequency are set to $F_0 = 1$ and $\Omega = 0.126$, respectively.
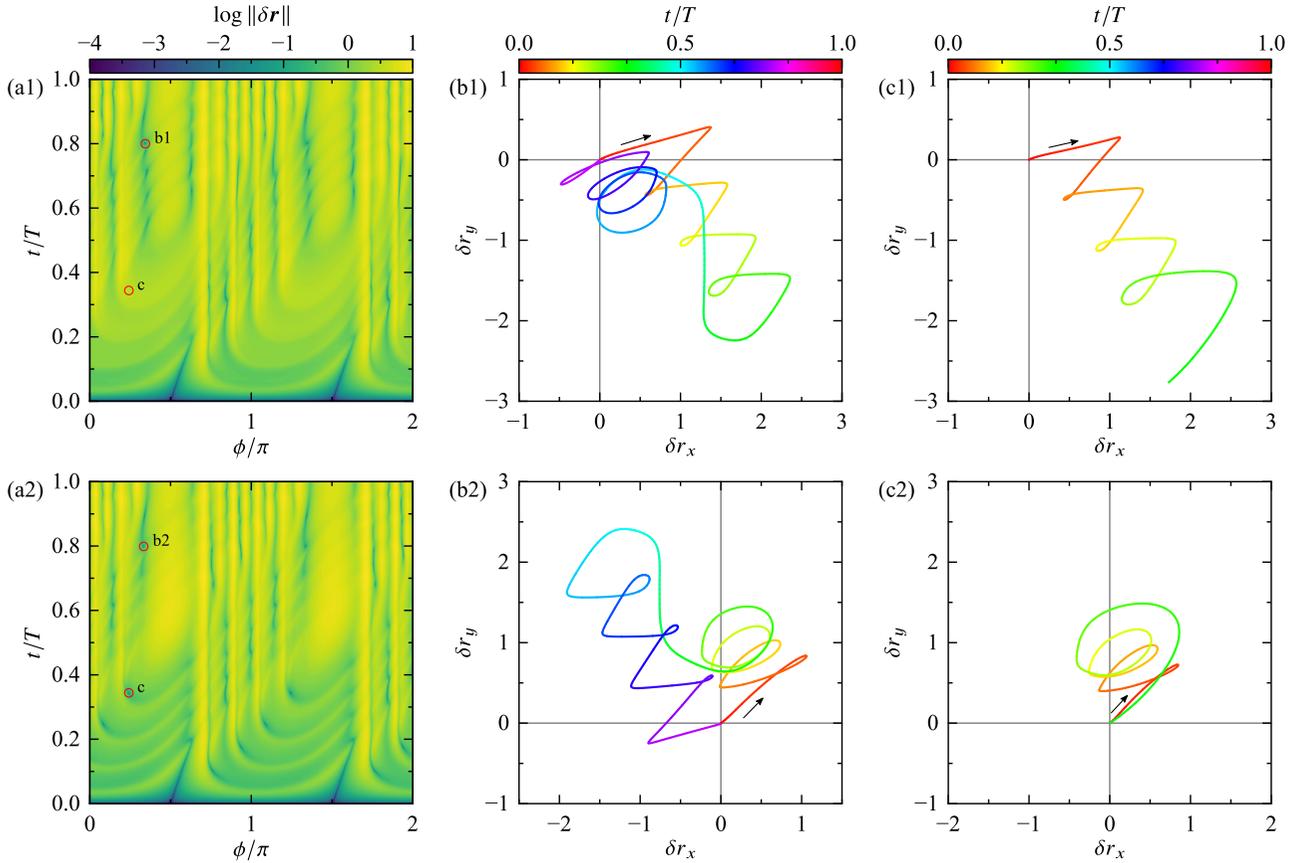
FIG. 7. Real-space dynamics of electron-hole pair excited at $t = 0$ with $\boldsymbol{k} = (0, 0)$, for $\chi = +\chi_0$ (top) and $\chi = -\chi_0$ (bottom). The electric field amplitude, frequency, polarization angle are set to $F_0 = 1$, $\Omega = 0.126$, and $\psi = 32°$, respectively. (a) Color map of the norm of the relative displacement, $\|\delta\boldsymbol{r}\|$, in the ϕ-t plane. (b) Real-space trajectory of $\delta\boldsymbol{r}$ until recombination for an initial phase indicated by the red circle, "b1" and "b2," in (a). (c) Same as (b) but for a different initial phase indicated by "c" in (a); point "c" in (a1) is not a local minimum of $\|\delta\boldsymbol{r}\|$, and thus in (c1), the pair does not recombine (see main text).

C. Electron-hole dynamics in real space

In the previous section, as shown in Fig. 6, it was revealed that the polarization angle dependence of harmonic intensity changes with the sign of scalar chirality, and that it is mostly due to the contribution of an electric current component parallel to the electric field. Since it is currently difficult to fully understand this cause microscopically, in this section, we discuss interband currents by analyzing a real-space trajectory of an electron-hole pair excited at a wave-number point $\boldsymbol{k} = \boldsymbol{k}_0$.

At half filling, optical driving primarily excites electrons into the third lowest band $\varepsilon_3(\boldsymbol{k})$, while creating holes in the second band $\varepsilon_2(\boldsymbol{k})$. Interband currents are induced when these electrons and holes recombine. In the saddle-point approximation [70–74], this condition is expressed as $\|\delta\boldsymbol{r}\| = 0$, where $\delta\boldsymbol{r}$ represents the relative displacement of the electron-hole pair excited at time $t = 0$. This displacement is given by

$$\delta\boldsymbol{r}(t) = \int_0^t \delta\dot{\boldsymbol{r}}(t') \, dt', \quad (25)$$

where $\delta\dot{\boldsymbol{r}}$ denotes the relative velocity of the electron-hole pair with momentum $\boldsymbol{k}$:

$$\delta\dot{\boldsymbol{r}} = \partial_{\boldsymbol{k}}[\varepsilon_3(\boldsymbol{k}) - \varepsilon_2(\boldsymbol{k})] + \boldsymbol{F}(t) \times [\boldsymbol{B}_3(\boldsymbol{k}) - \boldsymbol{B}_2(\boldsymbol{k})]. \quad (26)$$

The optical vector potential is introduced through the Peierls substitution: $\boldsymbol{k}(t) = \boldsymbol{k}_0 + \boldsymbol{A}(0) - \boldsymbol{A}(t)$ with $\boldsymbol{A}(t) = -(\boldsymbol{F}_0/\Omega) \sin(\Omega t - \phi)$. Therefore, by finding the phase ϕ for which $\|\delta\boldsymbol{r}\| = 0$ at time $t > 0$, we can determine the real-space trajectory of the electron-hole pair until recombination.

Analyzing all trajectories of electron-hole pairs for every $\boldsymbol{k}_0$ would only complicate the problem. Thus, here, we specifically show representative cases for a pair excited at $\boldsymbol{k}_0 = (0, 0)$, that is, at the Γ point. Figure 7(a) displays the relative displacement $\|\delta\boldsymbol{r}\|$ on a logarithmic scale as a function of the initial phase ϕ and time t, with Fig. 7(a1) for $\chi = +\chi_0$ and Fig. 7(a2) for $\chi = -\chi_0$. The polarization angle is set to $\psi = 32°$, for which the fifth-order harmonic intensity for $\chi = +\chi_0$ nearly reaches its maximum [see Fig. 6(c)]. Overall, both cases exhibit similar behaviors, but, reflecting the sign of scalar chirality (i.e., the sign of the Berry curvature), the details differ. There are specifically two cases in which the electron-hole pair can recombine: (i) for both $\chi = +\chi_0$ and $\chi = -\chi_0$, the pair recombines at almost the same phase ϕ and time t (indicated by points "b1" and "b2"), and (ii) the pair recombines only for either $\chi = +\chi_0$ or $\chi = -\chi_0$ (indicated by point "c"). We discuss these two cases in detail.

Case (i). The phase and the recombination time of points "b1" and "b2" in Figs. 7(a1) and 7(a2) are $\phi/\pi = 0.344$ and $t/T = 0.800$ for $\chi = +\chi_0$, and $\phi/\pi = 0.333$ and
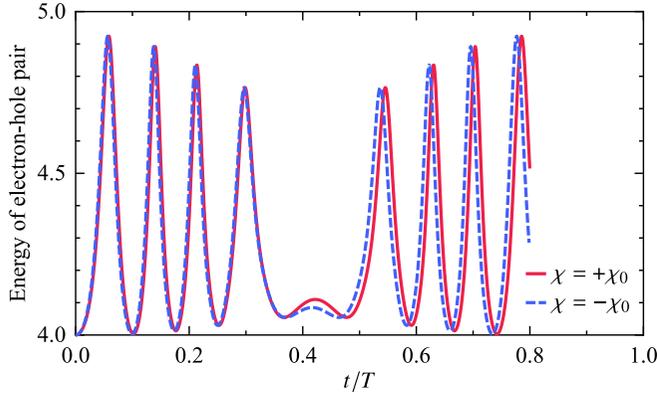
FIG. 8. Temporal profiles of the energy of electron-hole pair until the recombination, with the initial phases indicated by "b1" for $\chi = +\chi_0$ and by "b2" for $\chi = -\chi_0$ in Figs. 7(a1) and 7(a2) (see main text). The other parameters are the same as those in Fig. 7.

$t/T = 0.799$ for $\chi = -\chi_0$. Here, $T = 2\pi/\Omega = 50$ represents the optical period. The corresponding trajectories in real space are shown in Figs. 7(b1) and 7(b2). Although these trajectories are close to what would be expected if the time was reversed for the other, the contribution from the anomalous velocity term modifies the conditions for recombination. This results in a slight difference in a recombination energy. Figure 8 shows the temporal profile of the electron-hole pair's energy, $\varepsilon_3(\boldsymbol{k}(t)) - \varepsilon_2(\boldsymbol{k}(t))$, where we in fact observe the slight difference. Thus, in this case, while the electron-hole pair recombines for both $\chi = +\chi_0$ and $\chi = -\chi_0$, their different recombination energies at $t \approx 0.8$ yield a different harmonic intensity.

Case (ii). When $\phi/\pi = 0.2416$ and $t/T = 0.344$, indicated as "c" in Fig. 7(a), pair recombination occurs only for $\chi = -\chi_0$. The trajectories for this case are shown in Figs. 7(c1) and 7(c2). For $\chi = +\chi_0$, the electron-hole pair does not return to the coordinate origin, and thus, this pair does not contribute to interband currents.

From the two cases above, the reason why the dependence of the chirality sign, as shown in Fig. 6, appears as a longitudinal response can be inferred to be due to the difference in the dynamics of electron-hole pairs in real space. This difference is caused by the anomalous velocity, which also changes the recombination conditions. Furthermore, even in a case where recombination occur for both $\chi = +\chi_0$ and $\chi = -\chi_0$, the difference in the recombination energy results in variations in harmonic intensity. However, it is also important to note that the analysis conducted here is significantly simplified and does not consider crucial factors such as temporal changes in the carrier density and interference with other pairs excited at different $\boldsymbol{k}$'s, necessitating more comprehensive analyses as conducted in Ref. [89] in future work.

D. HHG with parameters for real materials

In the previous sections, we discussed the case where $J_K = 3$ and $n_e = 0.5$. Recently, some experiments reported that the four-sublattice scalar chiral state is realized in CoTa$_3$S$_6$ and CoNb$_3$S$_6$ [102–104]. Here, we discuss the high harmonic spectrum and its polarization angle dependence for parame-
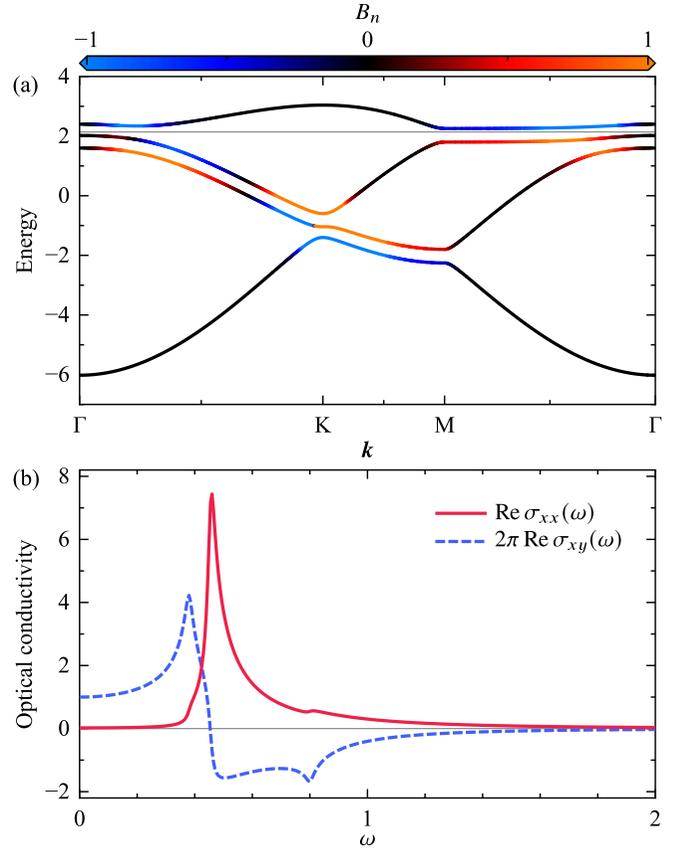
FIG. 9. (a) Energy band structure $\varepsilon_n(\boldsymbol{k})$ for $J_K = 0.4$ ($\chi = +\chi_0$). The color variation along the lines indicates the Berry curvature $B_n(\boldsymbol{k})$. The gray horizontal line shows the chemical potential $\mu = 2.137$ for $n_e = 0.75$. (b) Real part of optical conductivity in the scalar chiral state with $\chi = +\chi_0$ at zero temperature. The parameters are set to $J_K = 0.4$, $n_e = 0.75$, and $\eta = 0.01$.

ters close to these materials, with $J_K = 0.4$ and $n_e = 0.75$. We will see that the aforementioned conclusion regarding the dominance of the longitudinal response depending on the chirality sign also holds in this case.

Before moving on to the discussion of HHG, we present the equilibrium properties. Figure 9(a) shows the energy band structure and Berry curvature in the ground state for $J_K = 0.4$. Only at three-quarter filling ($n_e = 0.75$), the ground state is insulating. The optical conductivity is shown in Fig. 9(b). A significant absorption peak in $\sigma_{xx}(\omega)$ is observed near $\omega = 0.42$, corresponding to the transition between the upper two bands on the Γ–M line. Hereafter, the optical frequency will continue to be set at $\Omega = 0.126$, which is still lower than the optical gap. Furthermore, reflecting the Berry curvature, the optical Hall conductivity $\sigma_{xy}(\omega)$ also appears, and it reaches the quantized value of $+e^2/(2\pi\hbar)$ in the dc limit ($\omega \to 0$).

In Fig. 10, we show the power spectrum $I_\alpha(\omega)$ for $F_0 = 0.1$ and $\Omega = 0.126$. Similarly to Fig. 4(c), the transverse response I_y appears with the same order of magnitude as or several orders of magnitude smaller than the longitudinal response $I_x(\omega)$. As the energy range from the bottom to the top band edge is approximately 9 [see Fig. 9(a)], we observe the cutoff energy (i.e., the upper end of the plateau region) to be at the same energy ~8 in the spectrum.
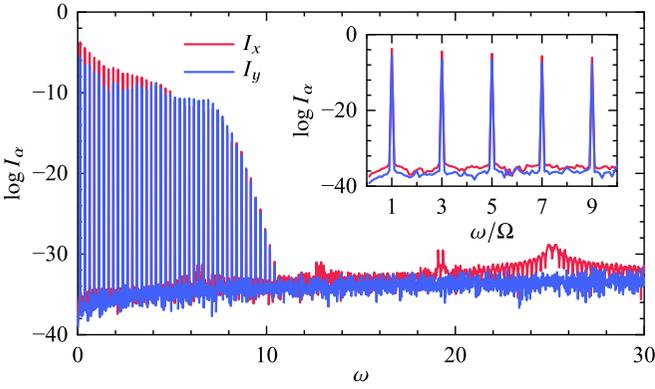
FIG. 10. Power spectra of the electric currents, $I_x(\omega)$ and $I_y(\omega)$. The inset shows the intensity of low-order harmonics. The parameters are set to $J_K = 0.4$, $n_e = 0.75$, $F_0 = 0.1$, $\Omega = 0.126$, and $N = 200^2$.

Figure 11(a) shows the color map of the intensity of odd-order harmonics for $\chi = +\chi_0$, as a function of the electric field amplitude. Reflecting the observation in Fig. 2(b) that the optical gap is about an order of magnitude smaller than that in the case of $J_K = 3$, the transition from the perturbative to the nonperturbative region occurs at a lower F_0. The intensity $I(\omega)$ is particularly strong in the region of $\omega \lesssim 10$, consistent with the bandwidth of the electrons. In addition, in the region below the white dashed line in Fig. 11(a), a significant contribution from intraband currents associated with the Bloch oscillation is also apparent.

The F_0 dependence of the harmonic intensities up to the ninth order is shown in Fig. 11(b). For the fundamental harmonic ($n = 1$), a deviation from the perturbative line $J_x(\Omega) \propto F_0$ can be seen above $F_0 \sim 0.1$, and for higher harmonics, this deviation can be seen at a smaller F_0. To consider the same situation as in the previous sections, the following discusses the polarization angle dependence for $F_0 = 0.1$.

We present the polarization angle dependence of harmonic intensity in Fig. 12. Similarly to the case of $J_K = 3$ and $n_e = 0.5$, the harmonic intensities depend on the polarization angle ψ, reflecting the sign of chirality. However, for harmonics up to the fifth order at $F_0 = 0.1$, the significant angle dependence shown in Figs. 6(c) and 6(d) are not observed. Additionally, the thin dashed lines in the figure indicates the longitudinal intensity $I_{\parallel}$ parallel to the electric field $\mathbf{F}_0$, which, as in the previous case, satisfies $I_{\parallel} \approx I$, indicating the dominance of the longitudinal response depending on the chirality sign. Therefore we consider that the results and discussions in the previous sections do not qualitatively depend on details such as model parameters or electron density.

IV. DISCUSSION

In Sec. III, we have focused particularly on a case where the optical frequency is significantly lower than the energy gap. Previous studies [80–86] have mainly discussed the effects of anomalous velocity in intraband currents; however, our results reveal that despite the dominance of the longitudinal response over the transverse response, the polarization angle dependence of harmonic intensity strongly reflects the
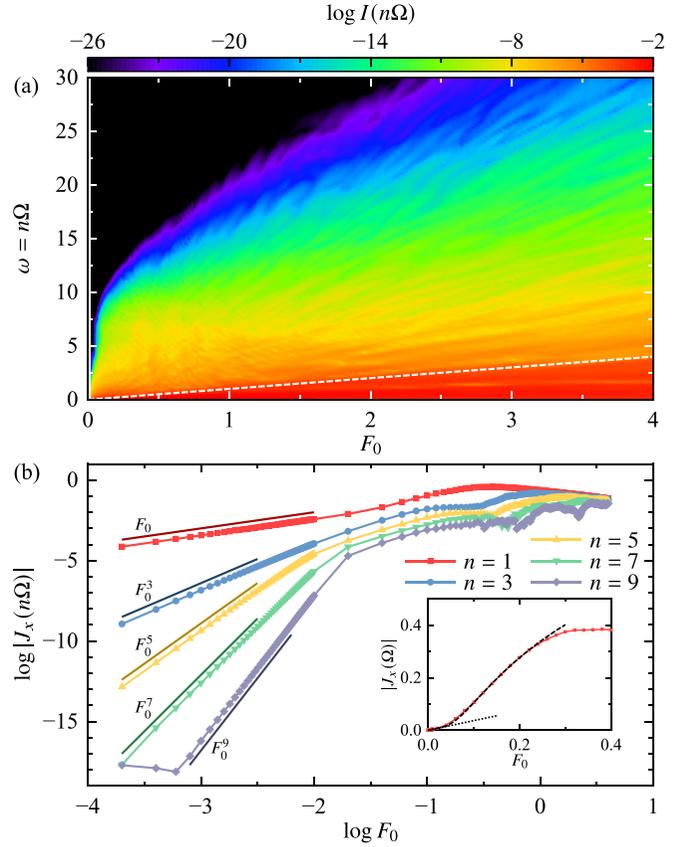
FIG. 11. (a) Amplitude dependence of the power spectrum of odd-order harmonics, $I(n\Omega)$ ($n = 1, 3, \ldots$). The dashed line indicates the upper bound of the Bloch oscillation frequency. (b) Fourier amplitude of low-order harmonics, $J_x(n\Omega)$, as a function of F_0. The inset shows $J_x(\Omega)$ on a linear scale, with the dashed curve representing a fitted function, $|J_x(\Omega)| = 0.3692 F_0 + 0.6032 \exp(-0.2177/F_0)$, and the dotted line being its linear component. The parameters are set to $J_K = 0.4$, $n_e = 0.75$, $\Omega = 0.126$, $\psi = 0$, and $N = 100^2$ in (a) and (b).

sign of scalar chirality. While this behavior might also be observed in systems with broken spatial inversion symmetry and nonzero Berry curvature, note that the sign of the Berry curvature can be easily switched by an external magnetic field in systems with broken time reversal symmetry.

It is also a natural question whether the anomalous velocity term in intraband currents (i.e., the transverse response) could dominate in the present system. In Appendix A, we show results on the polarization angle dependence in the case of near-resonant driving. There, indeed, the transverse response can become comparable to or greater than the longitudinal response. Besides, it is noteworthy that the longitudinal response still exhibits a dependence on the chirality sign. In addition, Appendices B and C respectively present brief summaries of the high harmonic spectrum in the case with circular polarization driving, and of the polarization angle dependence of the harmonic intensities in the 120° Néel state, where the Berry curvature is zero.

As already mentioned, the linear optical Hall effect with topological spin textures has been discussed in the literature [93–97]. In systems with sixfold symmetry like the one
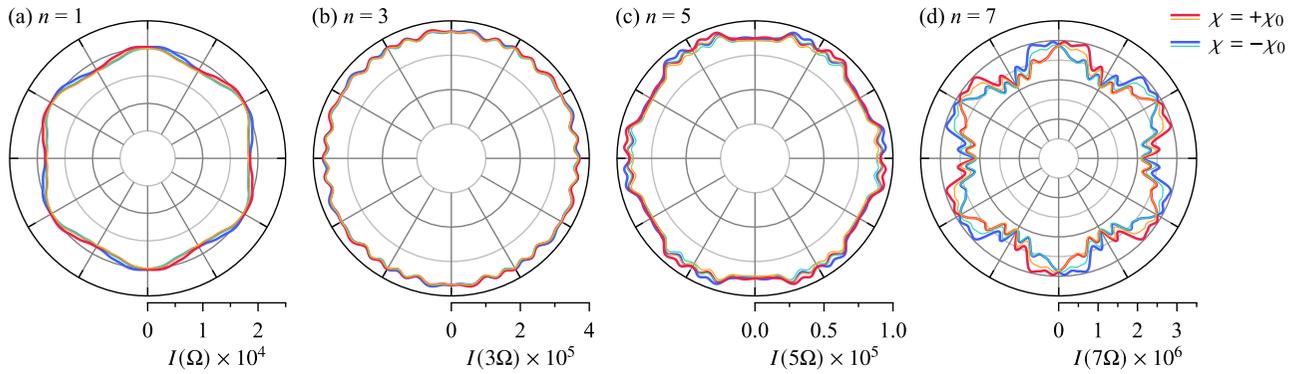
FIG. 12. [(a)–(d)] Polarization angle dependence of the nth harmonic intensity $I(n\Omega)$ for $\chi = +\chi_0$ (red) and $\chi = -\chi_0$ (blue). The thin curves show the longitudinal component $I_\parallel(n\Omega)$ for $\chi = +\chi_0$ (orange) and $\chi = -\chi_0$ (cyan). The parameters are set to $J_K = 0.4$, $n_e = 0.75$, $F_0 = 0.1$, and $\Omega = 0.126$.

considered here, the linear conductivity exhibits continuous rotational symmetry, and thus shows no polarization angle dependence, unlike what is observed in Figs. 6 and 12. Therefore, to verify the results presented in this paper, experiments need to be conducted on single crystals without grain boundaries. Additionally, the scalar chiral state in $CoTa_3S_6$ and $CoNb_3S_6$ is metallic [102–104], leading to the enhancement of the intraband-current response. Thus, examining harmonics in a frequency range higher than the Bloch oscillation frequency would facilitate a clearer observation of the contribution from interband currents.

V. SUMMARY

In this paper, we numerically analyzed HHG arising from electrons in the spin scalar chiral state. Reflecting the presence of the Berry curvature, the transverse response emerges, which is of the same order of magnitude as, or several orders of magnitude smaller than, the longitudinal response; its phase inversion depends on the sign of scalar chirality. Furthermore, we observed a marked variation in harmonic intensity with respect to the incident polarization angle, dependent on the chirality sign, with the dominant component being the longitudinal response rather than the transverse one. Since the anomalous velocity term in intraband currents produces only the transverse currents, this longitudinal response can be attributed to interband currents induced by the recombination of electron-hole pairs whose trajectories are modulated by the anomalous velocity. This modulation changes the recombination energies of the pairs and thus can alter the spectrum of interband currents. These results indicate that the magnetic structure with scalar chirality is, in fact, reflected in the high harmonic spectrum through the electron dynamics, which can be verified in experiments with materials such as $CoTa_3S_6$ and $CoNb_3S_6$, where the sign of scalar chirality can be switched by a magnetic field. Further research is expected to extend to HHG and HSG in systems with other topological spin textures, such as skyrmion lattice and hedgehog lattice states. Additionally, while the localized spins are fixed in this study, considering the dynamics resulting from the coupling between electrons and magnons would present an interesting direction [105,111–113].

APPENDIX A: NEAR-RESONANT DRIVING

In the main text, we set the optical frequency to $\Omega = 0.126$ and discussed the situation where it is significantly lower than the optical gap of 4 for $J_K = 3$. Here, we present in Fig. 13 the polarization angle dependence of harmonic intensity for a near-resonant case with $\Omega = 320 \times 2\pi/500 = 4.02$ and $F_0 = 1$. Since Ω is near resonant, the intensity of the fundamental harmonic is six orders of magnitude larger than that in Fig. 6(a), but the angle dependence is small, suggesting that its deviation from the perturbative regime is small. The higher order harmonics show a pronounced polarization angle dependence similar to the case of $\Omega = 0.126$, and changes relative to the sign of scalar chirality can be similarly observed. Among the higher order harmonics shown in Fig. 13, the third- and seventh-order longitudinal response satisfies $I_\parallel \approx I$, but for the fifth harmonic, the transverse response $I_\perp$ becomes comparable to or greater than $I_\parallel$. This large transverse response can be attributed to the anomalous velocity term in intraband currents, as discussed in the literature. Nevertheless, $I_\parallel$ still clearly depends on the chirality sign, indicating that $I(\omega)$ contains interband-current contributions discussed in Sec. III C.

APPENDIX B: CIRCULAR POLARIZATION DRIVING

Here, we briefly discuss HHG when circularly polarized light defined in Eq. (19) is applied. Before that, we present the relationship between the parameters of an ellipse and the electric current amplitude and phase. When the electric
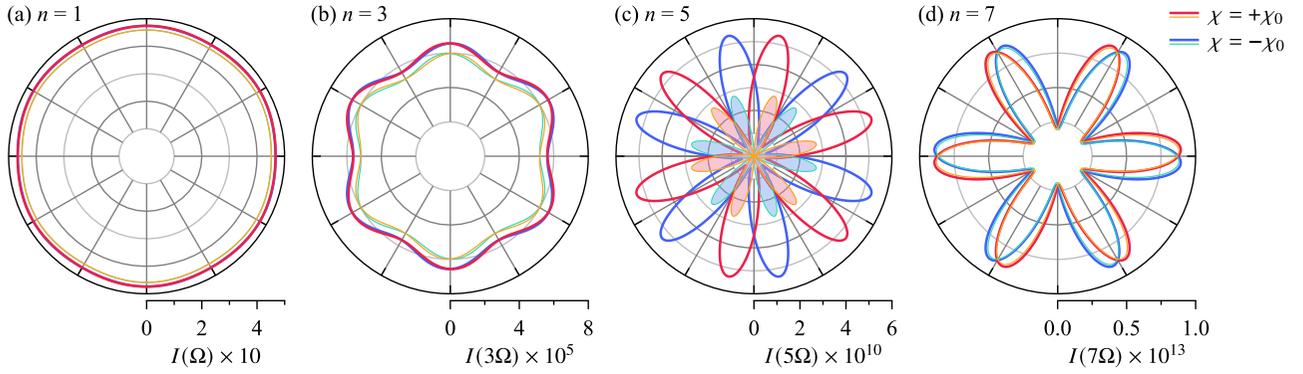
FIG. 13. [(a)–(d)] Polarization angle dependence of the nth harmonic intensity $I(n\Omega)$ for $\chi = +\chi_0$ (red) and $\chi = -\chi_0$ (blue). The thin curves show the longitudinal component $I_\parallel(n\Omega)$ for $\chi = +\chi_0$ (orange) and $\chi = -\chi_0$ (cyan), and $I_\parallel(5\Omega)$ is additionally shaded for visibility. The electric field amplitude and frequency are set to $F_0 = 1$ and $\Omega = 4.02$, respectively.

current corresponding to the nth harmonic is given by

$$J_\alpha(t) = J_{0,\alpha} \cos(n\Omega t - \phi_\alpha) \tag{B1}$$

with $J_{0,\alpha} = |J_\alpha(n\Omega)|$ and $\phi_\alpha = \arg J_\alpha(n\Omega)$, the trajectory on the J_x-J_y plane is an ellipse. Its semi-major axis J_+ and semi-minor axis J_- are respectively given by

$$J_+ = \max\{\tilde{J}_x, \tilde{J}_y\}, \quad J_- = \text{sgn}(\delta)\min\{\tilde{J}_x, \tilde{J}_y\}, \tag{B2}$$

where $\delta = \phi_y - \phi_x$ represents the relative phase, sgn denotes a sign function, and $\tilde{J}_x$ and $\tilde{J}_y$ are defined by

$$\tilde{J}_x = |\sin\delta| \left[\frac{\cos^2\varphi}{J_{0,x}^2} - \frac{\sin 2\varphi \cos\delta}{J_{0,x}J_{0,y}} + \frac{\sin^2\varphi}{J_{0,y}^2} \right]^{-\frac{1}{2}}, \tag{B3}$$

$$\tilde{J}_y = |\sin\delta| \left[\frac{\sin^2\varphi}{J_{0,x}^2} + \frac{\sin 2\varphi \cos\delta}{J_{0,x}J_{0,y}} + \frac{\cos^2\varphi}{J_{0,y}^2} \right]^{-\frac{1}{2}}. \tag{B4}$$

Here, φ represents the inclination angle of the ellipse's major axis with respect to the x axis, which is given by

$$\varphi = \frac{1}{2}\arctan\frac{2J_{0,x}J_{0,y}\cos\delta}{J_{0,x}^2 - J_{0,y}^2}. \tag{B5}$$

The ellipticity ϵ is defined by

$$\epsilon = -\frac{J_-}{J_+}, \tag{B6}$$

such that it equals $+1$ for RCP and -1 for LCP.

Figure 14(a) shows the power spectrum $I(\omega)$ for harmonics with intensity sufficiently separated from the background ($\lesssim 10^{-30}$). It is established that the allowed harmonics for a given crystal symmetry and optical-field waveform are described by a theory of dynamical symmetry [35,114–118]. In the present system, which exhibits sixfold symmetry, only the $(6l \pm 1)$th-order harmonics ($l \in \mathbb{Z}$) are allowed when circularly polarized light is applied, and our results are in agreement with this theoretical prediction. Additionally, Fig. 14(b) demonstrates that the ellipticity ϵ of each harmonic is determined solely by the handedness of the circular polarization, regardless of the sign of chirality. Furthermore, a kind of circular dichroism is observed; that is, for $\chi = +\chi_0$, the intensity of the fifth- to 13th-order harmonics under LCP is more pronounced than those under RCP, and this difference in intensities is inverted when the sign of chirality is altered.

APPENDIX C: COMPARISON WITH THE 120° NÉEL STATE

The 120° Néel state exhibits a three-sublattice magnetic order, which is stabilized at $n_e = 0.5$ in the present model [101]. The vector of the mth sublattice spin is defined by $\boldsymbol{S}_m = (\cos\theta_m, \sin\theta_m, 0)$ with $\theta_1 = 0$, $\theta_2 = 2\pi/3$, and $\theta_3 = -2\pi/3$. Given this configuration, the electron system is invariant under the combination of a mirror reflection with respect to the xy plane and the time reversal operation; thereby the Berry curvature $\boldsymbol{B}_n(\boldsymbol{k})$ satisfies $B_n^z(-k_x, -k_y, k_z) = -B_n^z(k_x, k_y, k_z)$ [119], or in two dimensions, $B_n(-k_x, -k_y) = -B_n(k_x, k_y)$.
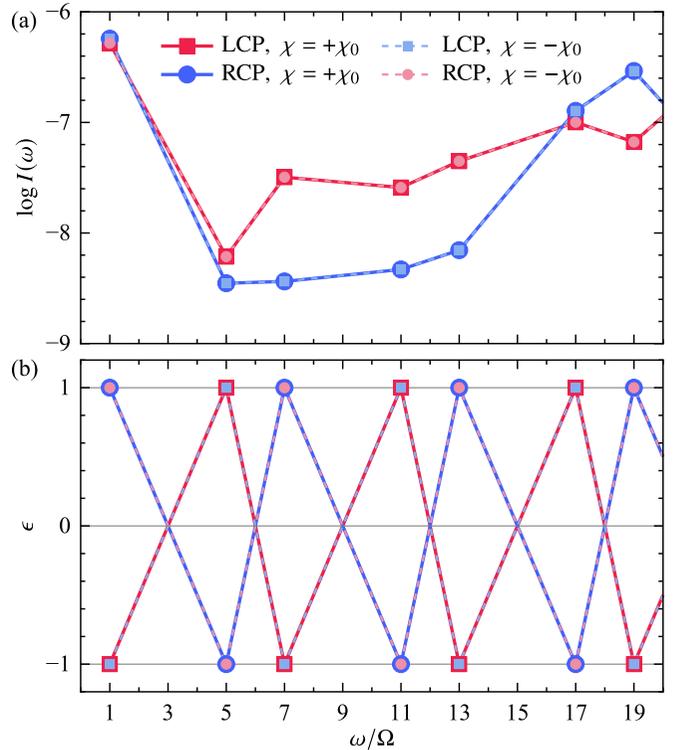
FIG. 14. (a) Power spectrum $I(\omega)$ and (b) ellipticity ϵ, for $(6l \pm 1)$th-order harmonics. RCP and LCP correspond to $\epsilon = +1$ and $\epsilon = -1$, respectively. The parameters are set to $J_K = 3$, $n_e = 0.5$, $F_0 = 0.1$, and $\Omega = 0.126$.

(a) $n = 3$
(b) $n = 5$

— I
— $I_\parallel$
— $I_\perp$

$\times 20$

$0 \quad 1 \quad 2 \quad 3$
$I(3\Omega) \times 10^9$

$0 \quad 2 \quad 4 \quad 6$
$I(5\Omega) \times 10^{11}$
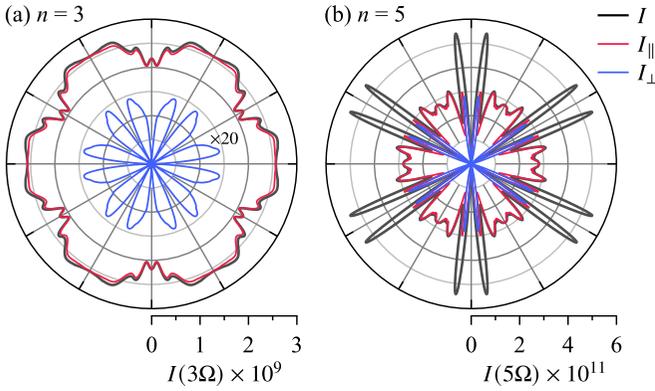
FIG. 15. Polarization angle dependence of the (a) third and (b) fifth harmonic intensity. The red and blue lines represent the longitudinal ($I_\parallel$) and transverse ($I_\perp$) component, respectively. For visibility, $I_\perp(3\Omega)$ in (a) is multiplied by 20.

Additionally, the presence of spatial inversion symmetry imposes $B_n(-k_x, -k_y) = B_n(k_x, k_y)$. Therefore the Berry curvature $B_n(\boldsymbol{k})$ turns out to be zero for any $\boldsymbol{k}$. In the case with $J_K = 3$ and $n_e = 0.5$ as adopted in the main text, the ground state is insulating, and the optical gap is $2J_K = 6$.

In Fig. 15, we present the polarization angle dependence of the third- and fifth-order harmonic intensities for $F_0 = 1$ and $\Omega = 0.126$, along with their longitudinal and transverse components. Similarly to the case in the four-sublattice scalar chiral state, sixfold symmetric harmonic intensity is observed, with the fifth harmonic showing more pronounced angle dependence. The transverse component $I_\perp$, shown in blue lines in the figure, appears except in the high symmetric directions such as $\psi = 0$ and $\psi = \pi/6$, and it does not depend on the sign of J_K unlike in the scalar chiral state. Such transverse response can be attributed to the first term of Eq. (22), $\partial_{\boldsymbol{k}} \varepsilon_n(\boldsymbol{k})$, having components that are not parallel to the momentum $\boldsymbol{k}$.

APPENDIX D: NONLINEAR RESPONSE IN THE PERTURBATIVE REGIME

We derive the perturbative expressions for the harmonic intensity and discuss the polarization angle dependence. In general, the nth-order response of the electric current $\boldsymbol{J}$ to the electric field $\boldsymbol{F}$ is given by

$$J_\alpha^{(n)}(\omega) = \int_{-\infty}^{\infty} \frac{d\omega_1 \cdots d\omega_n}{(2\pi)^{n-1}} \delta(\omega_1 + \cdots + \omega_n - \omega)$$
$$\times \sigma_{\alpha\alpha_1\cdots\alpha_n}^{(n)}(\omega_1, \ldots, \omega_n) F_{\alpha_1}(\omega_1) \cdots F_{\alpha_n}(\omega_n), \quad \text{(D1)}$$

where $\sigma^{(n)}$ is the nth-order response function, α and $\alpha_{i=1,\ldots,n}$ indicate Cartesian components (such as x and y), and summation over repeated indices (Einstein summation convention) is assumed. By definition, $\sigma^{(n)}$ is invariant under the permutation of $(\alpha_i, \omega_i) \leftrightarrow (\alpha_j, \omega_j)$, and thus, it is convenient to introduce the nth-order symmetrized response function:

$$\bar{\sigma}_{\alpha\alpha_1\cdots\alpha_n}^{(n)}(\omega_1, \ldots, \omega_n)$$
$$= \sum_{s \in \mathfrak{S}_n} \sigma_{\alpha\alpha_{s(1)}\cdots\alpha_{s(n)}}^{(n)}(\omega_{s(1)}, \ldots, \omega_{s(n)}), \quad \text{(D2)}$$

where $\mathfrak{S}_n$ is the symmetric group of degree n. For example, when $n = 2$, Eq. (D2) is written as $\bar{\sigma}_{\alpha\alpha_1\alpha_2}^{(2)}(\omega_1, \omega_2) = \sigma_{\alpha\alpha_1\alpha_2}^{(2)}(\omega_1, \omega_2) + \sigma_{\alpha\alpha_2\alpha_1}^{(2)}(\omega_2, \omega_1)$. Additionally, if the system is invariant under a symmetry operation represented by a unitary matrix U, the response function satisfies the relation:

$$\sigma_{\alpha\alpha_1\cdots\alpha_n}^{(n)} = U_{\alpha\beta} U_{\alpha_1\beta_1} \cdots U_{\alpha_n\beta_n} \sigma_{\beta\beta_1\cdots\beta_n}^{(n)}, \quad \text{(D3)}$$

which reduces the number of independent nonzero components of $\sigma_{\alpha\alpha_1\cdots\alpha_n}^{(n)}$.

Given that the present system preserves sixfold symmetry, we obtain from Eq. (D3) the well-known relations,

$$\sigma_{xx}^{(1)} = \sigma_{yy}^{(1)}, \quad \sigma_{xy}^{(1)} = -\sigma_{yx}^{(1)} \quad \text{(D4)}$$

for the first-order response. Such relations can also be derived for higher-order responses, while we do not write them all out. Instead, here we discuss the polarization angle dependence of the nth harmonic intensity, assuming the linearly polarized electric field,

$$\boldsymbol{F}(\omega) = 2\pi \delta(\omega - \Omega)\boldsymbol{F}_0, \quad \boldsymbol{F}_0 = F_0(\cos\psi, \sin\psi). \quad \text{(D5)}$$

Here, F_0 and Ω represent the amplitude and frequency of the electric field, respectively, and ψ denotes the polarization angle as in Eq. (18). Under this assumption, the nth-order response in Eq. (D1) reduces to

$$J_\alpha^{(n)}(\omega) = 2\pi \delta(\omega - n\Omega)\sigma_{\alpha\alpha_1\cdots\alpha_n}^{(n)} F_{0,\alpha_1} \cdots F_{0,\alpha_n}, \quad \text{(D6)}$$

$$J_\alpha^{(n)}(t) = \int_{-\infty}^{\infty} \frac{d\omega}{2\pi} e^{-i\omega t} J_\alpha^{(n)}(\omega)$$
$$= e^{-in\Omega t} \sigma_{\alpha\alpha_1\cdots\alpha_n}^{(n)} F_{0,\alpha_1} \cdots F_{0,\alpha_n}$$
$$= e^{-i(n\Omega t - \phi_\alpha^{(n)})} |J_{0,\alpha}^{(n)}|, \quad \text{(D7)}$$

where

$$J_{0,\alpha}^{(n)} = \sigma_{\alpha\alpha_1\cdots\alpha_n}^{(n)} F_{0,\alpha_1} \cdots F_{0,\alpha_n}, \quad \phi_\alpha^{(n)} = \arg J_{0,\alpha}^{(n)}, \quad \text{(D8)}$$

and $\sigma_{\alpha\alpha_1\cdots\alpha_n}^{(n)}$ is a shorthand for $\sigma_{\alpha\alpha_1\cdots\alpha_n}^{(n)}(\Omega, \ldots, \Omega)$. Consequently, the nth harmonic intensity is given by

$$I(n\Omega) = (n\Omega)^2 \left(|J_{0,x}^{(n)}|^2 + |J_{0,y}^{(n)}|^2 \right). \quad \text{(D9)}$$

By using Eqs. (D3) and (D5)–(D9), we obtain an expression for the first-order harmonic intensity,

$$I(\Omega) \propto \left(|\sigma_{xx}^{(1)}|^2 + |\sigma_{xy}^{(1)}|^2 \right) F_0^2, \quad \text{(D10)}$$

which is independent of ψ as mentioned in the main text. Similarly, the third harmonic intensity, written as

$$I(3\Omega) \propto \left(|\bar{\sigma}_{xxxx}^{(3)}|^2 + |\bar{\sigma}_{xxxy}^{(3)}|^2 \right) F_0^6, \quad \text{(D11)}$$

is also independent of ψ. However, the fifth harmonic intensity turns out to be

$$I(5\Omega) \propto [C_0 + C_+ \cos(6\psi) + C_- \sin(6\psi)] F_0^{10}, \quad \text{(D12)}$$

which exhibits sixfold symmetry in the perturbative regime and reaches its maximum when $6\psi = \arctan(C_-/C_+) \bmod 2\pi$. Here, C_0, C_+, and C_- are constants given by

$$C_0 = 117|\bar{\sigma}_{yyyxxx}^{(5)}|^2 + 432|\bar{\sigma}_{yyyxxx}^{(5)} \bar{\sigma}_{yyyyyx}^{(5)}| + 468|\bar{\sigma}_{yyyyyx}^{(5)}|^2$$
$$+ 25\left(|\bar{\sigma}_{yyyyxx}^{(5)}|^2 + 8|\bar{\sigma}_{yyyyxx}^{(5)} \bar{\sigma}_{yyyyyy}^{(5)}| + 52|\bar{\sigma}_{yyyyyy}^{(5)}|^2 \right), \quad \text{(D13)}$$

$$C_+ = -45\left|\bar{\sigma}^{(5)}_{yyyxxx}\right|^2 + 180\left|\bar{\sigma}^{(5)}_{yyyyyx}\right|^2$$
$$+ 25\left(\left|\bar{\sigma}^{(5)}_{yyyyxx}\right| - 2\left|\bar{\sigma}^{(5)}_{yyyyyy}\right|\right)\left(\left|\bar{\sigma}^{(5)}_{yyyyyx}\right| + 10\left|\bar{\sigma}^{(5)}_{yyyyyy}\right|\right),$$
$$\text{(D14)}$$

$$C_- = -90\left|\bar{\sigma}^{(5)}_{yyyxxx}\bar{\sigma}^{(5)}_{yyyyyx}\right|$$
$$- 120\left|\bar{\sigma}^{(5)}_{yyyyyx}\right|\left(\left|\bar{\sigma}^{(5)}_{yyyyyx}\right| - 5\left|\bar{\sigma}^{(5)}_{yyyyyy}\right|\right). \quad \text{(D15)}$$

For the seventh harmonic intensity, we find that

$$I(7\Omega) \propto [D_0 + D_{1+}\cos(6\psi) + D_{1-}\sin(6\psi)$$
$$+ D_{2+}\cos(12\psi) + D_{2-}\sin(12\psi)]F_0^{14}, \quad \text{(D16)}$$

where D_0, $D_{1\pm}$, and $D_{2\pm}$ are constants depending on $\sigma^{(7)}$. Note that Eqs. (D10)–(D16) are perturbative expressions valid in the limit of $F_0 \to 0$ and are derived solely from the six-fold symmetry, without making any additional assumptions regarding the electronic or magnetic structure.

Figure 16(a) shows the polarization angle dependence of the third and fifth harmonics for $F_0 = 0.01$. At this value of F_0, the response is within the perturbative regime, as evidenced by Fig. 5(b). In fact, the numerical results exhibit continuous rotational symmetry for the third harmonic and sixfold symmetry for the fifth harmonic, which are consistent with Eqs. (D11) and (D12).

We also notice that, in Fig. 16(a), while the third harmonic intensity becomes independent of the chirality sign as $F_0 \to 0$, the fifth harmonic intensities show a slight difference between the cases of $\chi = +\chi_0$ and $-\chi_0$. When the electric-field amplitude is finite, F_0-dependent terms enter Eqs. (D13)–(D15) through higher-order processes. Thus, to clarify whether the slight chirality-sign dependence observed in the fifth harmonic persists in the limit of $F_0 \to 0$, it is necessary to examine the dependence on F_0. In Fig. 16(b), the polarization angle at which $I(5\Omega)$ is maximized is plotted as a function of F_0, and it deviates from the x-axis by ∓ 0.0113 rad $= \mp 0.65°$ for $\chi = \pm\chi_0$ in the limit of $F_0 \to 0$. Since this deviation is quite small, the significant chirality-sign dependence observed in Figs. 6, 12, and 13, as well as the pronounced polarization angle dependence with a nodelike structure, is likely enhanced by nonperturbative effects.

To further validate that the polarization angle dependence observed in Fig. 16(a) can be described perturbatively, we consider the difference between the harmonic intensities for $\psi = 0$ and $\psi = \pi/6$:

$$\delta I^{(n)} = I(n\Omega)|_{\psi=0} - I(n\Omega)|_{\psi=\pi/6}. \quad \text{(D17)}$$

Figure 16(c) presents $\delta I^{(n)}$ on a logarithmic scale for $n = 1$ to 9. For the first and third harmonics, we observe that

$$\delta I^{(1)} \propto F_0^6 = o(F_0^2), \quad \delta I^{(3)} \propto F_0^8 = o(F_0^6). \quad \text{(D18)}$$

This suggests that a weak angle dependence, vanishing in the limit of $F_0 \to 0$, arises from higher-order perturbative processes. On the other hand, for the fifth and higher harmonics,
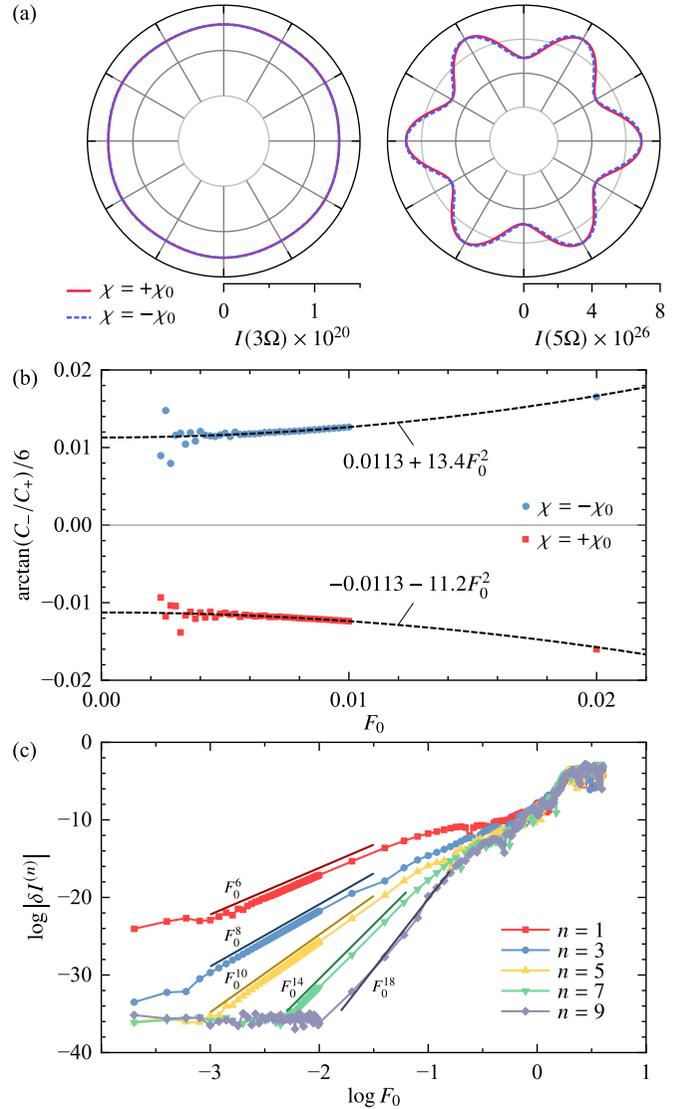
FIG. 16. (a) Polarization angle dependence of the third (left) and fifth (right) harmonic intensity in the perturbative regime, $F_0 = 0.01$. (b) Amplitude dependence of the polarization angle at which the fifth harmonic intensity $I(5\Omega)$ is maximized. The dashed curves represent quadratic fits to the data points for $F_0 \in [0.006, 0.01]$. (c) Amplitude dependence of $\delta I^{(n)}$ in Eq. (D17) when $\chi = +\chi_0$. The parameters are set to $J_K = 3$, $n_e = 0.5$, and $\Omega = 0.126$ in (a)–(c).

we see that

$$\delta I^{(n)} \propto F_0^{2n}, \quad \text{(D19)}$$

which indicates that the angle dependence remains even in the limit of $F_0 \to 0$. The above discussion and the numerical results shown in Fig. 16 explain why the nodelike structure observed for the fifth and seventh harmonics in Figs. 6 and 13 is absent for the first and third harmonics; that is, when $F_0 = 1$, the first- and third-order responses are still near the perturbative regime, as tunneling excitation is negligible.

[1] P. Agostini and L. F. DiMauro, The physics of attosecond light pulses, Rep. Prog. Phys. **67**, 813 (2004).

[2] L. Gallmann, C. Cirelli, and U. Keller, Attosecond science: Recent highlights and future trends, Annu. Rev. Phys. Chem. **63**, 447 (2012).

[3] F. Krausz and M. Ivanov, Attosecond physics, Rev. Mod. Phys. **81**, 163 (2009).

[4] S. Y. Kruchinin, F. Krausz, and V. S. Yakovlev, Colloquium: Strong-field phenomena in periodic systems, Rev. Mod. Phys. **90**, 021002 (2018).

[5] S. Ghimire and D. A. Reis, High-harmonic generation from solids, Nat. Phys. **15**, 10 (2019).

[6] K. Amini, J. Biegert, F. Calegari, A. Chacón, M. F. Ciappina, A. Dauphin, D. K. Efimov, C. Figueira de Morisson Faria, K. Giergiel, P. Gniewek, A. S. Landsman, M. Lesiuk, M. Mandrysz, A. S. Maxwell, R. Moszyński, L. Ortmann, J. Antonio Pérez-Hernández, A. Picón, E. Pisanty, J. Prauzner-Bechcicki *et al.*, Symphony on strong field approximation, Rep. Prog. Phys. **82**, 116001 (2019).

[7] L. Li, P. Lan, X. Zhu, and P. Lu, High harmonic generation in solids: particle and wave perspectives, Rep. Prog. Phys. **86**, 116401 (2023).

[8] M. Borsch, M. Meierhofer, R. Huber, and M. Kira, Lightwave electronics in condensed matter, Nat. Rev. Mater. **8**, 668 (2023).

[9] M. Na, A. K. Mills, and D. J. Jones, Advancing time- and angle-resolved photoemission spectroscopy: The role of ultrafast laser development, Phys. Rep. **1036**, 1 (2023).

[10] A. de la Torre, D. M. Kennes, M. Claassen, S. Gerber, J. W. McIver, and M. A. Sentef, Colloquium: Nonthermal pathways to ultrafast control in quantum materials, Rev. Mod. Phys. **93**, 041002 (2021).

[11] D. Filippetto, P. Musumeci, R. K. Li, B. J. Siwick, M. R. Otto, M. Centurion, and J. P. F. Nunes, Ultrafast electron diffraction: Visualizing dynamic states of matter, Rev. Mod. Phys. **94**, 045004 (2022).

[12] F. Boschini, M. Zonno, and A. Damascelli, Time-resolved ARPES studies of quantum materials, Rev. Mod. Phys. **96**, 015003 (2024).

[13] T. Oka and S. Kitamura, Floquet engineering of quantum materials, Annu. Rev. Condens. Matter Phys. **10**, 387 (2019).

[14] Y. Murakami, D. Golež, M. Eckstein, and P. Werner, Photo-induced nonequilibrium states in Mott insulators, arXiv:2310.05201.

[15] S. Ghimire, A. D. DiChiara, E. Sistrunk, P. Agostini, L. F. DiMauro, and D. A. Reis, Observation of high-order harmonic generation in a bulk crystal, Nat. Phys. **7**, 138 (2011).

[16] O. Schubert, M. Hohenleutner, F. Langer, B. Urbanek, C. Lange, U. Huttner, D. Golde, T. Meier, M. Kira, S. W. Koch, and R. Huber, Sub-cycle control of terahertz high-harmonic generation by dynamical Bloch oscillations, Nat. Photonics **8**, 119 (2014).

[17] M. Hohenleutner, F. Langer, O. Schubert, M. Knorr, U. Huttner, S. W. Koch, M. Kira, and R. Huber, Real-time observation of interfering crystal electrons in high-harmonic generation, Nature (London) **523**, 572 (2015).

[18] M. Garg, M. Zhan, T. T. Luu, H. Lakhotia, T. Klostermann, A. Guggenmos, and E. Goulielmakis, Multi-petahertz electronic metrology, Nature (London) **538**, 359 (2016).

[19] F. Langer, M. Hohenleutner, C. P. Schmid, C. Poellmann, P. Nagler, T. Korn, C. Schüller, M. S. Sherwin, U. Huttner, J. T. Steiner, S. W. Koch, M. Kira, and R. Huber, Lightwave-driven quasiparticle collisions on a subcycle timescale, Nature (London) **533**, 225 (2016).

[20] F. Langer, M. Hohenleutner, U. Huttner, S. W. Koch, M. Kira, and R. Huber, Symmetry-controlled temporal structure of high-harmonic carrier fields from a bulk crystal, Nat. Photonics **11**, 227 (2017).

[21] N. Yoshikawa, T. Tamaya, and K. Tanaka, High-harmonic generation in graphene enhanced by elliptically polarized light excitation, Science **356**, 736 (2017).

[22] M. S. Mrudul and G. Dixit, High-harmonic generation from monolayer and bilayer graphene, Phys. Rev. B **103**, 094308 (2021).

[23] P. Xia, T. Tamaya, C. Kim, F. Lu, T. Kanai, N. Ishii, J. Itatani, H. Akiyama, and T. Kato, High-harmonic generation in GaAs beyond the perturbative regime, Phys. Rev. B **104**, L121202 (2021).

[24] T. Tamaya, A. Ishikawa, T. Ogawa, and K. Tanaka, Diabatic mechanisms of higher-order harmonic generation in solid-state materials under high-intensity electric fields, Phys. Rev. Lett. **116**, 016601 (2016).

[25] S. A. Sato, H. Hirori, Y. Sanari, Y. Kanemitsu, and A. Rubio, High-order harmonic generation in graphene: Nonlinear coupling of intraband and interband transitions, Phys. Rev. B **103**, L041408 (2021).

[26] Y. Murakami and M. Schüler, Doping and gap size dependence of high-harmonic generation in graphene: Importance of consistent formulation of light-matter coupling, Phys. Rev. B **106**, 035204 (2022).

[27] Y. Murakami, K. Nagai, and A. Koga, Efficient control of high harmonic terahertz generation in carbon nanotubes using the Aharonov-Bohm effect, Phys. Rev. B **108**, L241202 (2023).

[28] I. Floss, C. Lemell, G. Wachter, V. Smejkal, S. A. Sato, X.-M. Tong, K. Yabana, and J. Burgdörfer, *Ab initio* multiscale simulation of high-order harmonic generation in solids, Phys. Rev. A **97**, 011401(R) (2018).

[29] F. Sekiguchi, M. Sakamoto, K. Nakagawa, H. Tahara, S. A. Sato, H. Hirori, and Y. Kanemitsu, Enhancing high harmonic generation in GaAs by elliptically polarized light excitation, Phys. Rev. B **108**, 205201 (2023).

[30] J. Kono, M. Y. Su, T. Inoshita, T. Noda, M. S. Sherwin, S. J. Allen, Jr., and H. Sakaki, Resonant terahertz optical sideband generation from confined magnetoexcitons, Phys. Rev. Lett. **79**, 1758 (1997).

[31] B. Zaks, R. B. Liu, and M. S. Sherwin, Experimental observation of electron-hole recollisions, Nature (London) **483**, 580 (2012).

[32] F. Langer, C. P. Schmid, S. Schlauderer, M. Gmitra, J. Fabian, P. Nagler, C. Schüller, T. Korn, P. G. Hawkins, J. T. Steiner, U. Huttner, S. W. Koch, M. Kira, and R. Huber, Lightwave valleytronics in a monolayer of tungsten diselenide, Nature (London) **557**, 76 (2018).

[33] K. Uchida, T. Otobe, T. Mochizuki, C. Kim, M. Yoshita, K. Tanaka, H. Akiyama, L. N. Pfeiffer, K. W. West, and H. Hirori, Coherent detection of THz-induced sideband emission from excitons in the nonperturbative regime, Phys. Rev. B **97**, 165122 (2018).

[34] M. Borsch, C. P. Schmid, L. Weigl, S. Schlauderer, N. Hofmann, C. Lange, J. T. Steiner, S. W. Koch, R. Huber, and M. Kira, Super-resolution lightwave tomography of electronic bands in quantum materials, Science **370**, 1204 (2020).

[35] K. Nagai, K. Uchida, N. Yoshikawa, T. Endo, Y. Miyata, and K. Tanaka, Dynamical symmetry of strongly light-driven electronic system in crystalline solids, Commun. Phys. **3**, 137 (2020).

[36] J. B. Costello, S. D. O'Hara, Q. Wu, D. C. Valovcin, L. N. Pfeiffer, K. W. West, and M. S. Sherwin, Reconstruction of Bloch wavefunctions of holes in a semiconductor, Nature (London) **599**, 57 (2021).

[37] K. Uchida and K. Tanaka, High harmonic Mach–Zehnder interferometer for probing sub-laser-cycle electron dynamics in solids, Optica **11**, 1130 (2024).

[38] R. E. F. Silva, I. V. Blinov, A. N. Rubtsov, O. Smirnova, and M. Ivanov, High-harmonic spectroscopy of ultrafast many-body dynamics in strongly correlated systems, Nat. Photonics **12**, 266 (2018).

[39] Y. Murakami, M. Eckstein, and P. Werner, High-harmonic generation in mott insulators, Phys. Rev. Lett. **121**, 057405 (2018).

[40] S. Imai, A. Ono, and S. Ishihara, High harmonic generation in a correlated electron system, Phys. Rev. Lett. **124**, 157404 (2020).

[41] N. Tancogne-Dejean, M. A. Sentef, and A. Rubio, Ultrafast modification of hubbard U in a strongly correlated material: *Ab initio* high-harmonic generation in nio, Phys. Rev. Lett. **121**, 097402 (2018).

[42] O. Grånäs, I. Vaskivskyi, X. Wang, P. Thunström, S. Ghimire, R. Knut, J. Söderström, L. Kjellsson, D. Turenne, R. Y. Engel, M. Beye, J. Lu, D. J. Higley, A. H. Reid, W. Schlotter, G. Coslovich, M. Hoffmann, G. Kolesov, C. Schüßler-Langeheine, A. Styervoyedov *et al.*, Ultrafast modification of the electronic structure of a correlated insulator, Phys. Rev. Res. **4**, L032030 (2022).

[43] T. Nag, R.-j. Slager, T. Higuchi, and T. Oka, Dynamical synchronization transition in interacting electron systems, Phys. Rev. B **100**, 134301 (2019).

[44] Y. Murakami, S. Takayoshi, A. Koga, and P. Werner, High-harmonic generation in one-dimensional Mott insulators, Phys. Rev. B **103**, 035110 (2021).

[45] C. Orthodoxou, A. Zaïr, and G. H. Booth, High harmonic generation in two-dimensional Mott insulators, npj Quantum Mater. **6**, 76 (2021).

[46] M. Lysne, Y. Murakami, and P. Werner, Signatures of bosonic excitations in high-harmonic spectra of Mott insulators, Phys. Rev. B **101**, 195139 (2020).

[47] M. R. Bionta, E. Haddad, A. Leblanc, V. Gruson, P. Lassonde, H. Ibrahim, J. Chaillou, N. Émond, M. R. Otto, Á. Jiménez-Galán, R. E. F. Silva, M. Ivanov, B. J. Siwick, M. Chaker, and F. Légaré, Tracking ultrafast solid-state dynamics using high harmonic spectroscopy, Phys. Rev. Res. **3**, 023250 (2021).

[48] C. Shao, H. Lu, X. Zhang, C. Yu, T. Tohyama, and R. Lu, High-harmonic generation approaching the quantum critical point of strongly correlated systems, Phys. Rev. Lett. **128**, 047401 (2022).

[49] M. Udono, K. Sugimoto, T. Kaneko, and Y. Ohta, Excitonic effects on high-harmonic generation in Mott insulators, Phys. Rev. B **105**, L241108 (2022).

[50] T. Hansen, S. V. B. Jensen, and L. B. Madsen, Correlation effects in high-order harmonic generation from finite systems, Phys. Rev. A **105**, 053118 (2022).

[51] T. Hansen and L. B. Madsen, Doping effects in high-harmonic generation from correlated systems, Phys. Rev. B **106**, 235142 (2022).

[52] K. Uchida, G. Mattoni, S. Yonezawa, F. Nakamura, Y. Maeno, and K. Tanaka, High-order harmonic generation and its unconventional scaling law in the mott-insulating Ca_2RuO_4, Phys. Rev. Lett. **128**, 127401 (2022).

[53] Y. Murakami, K. Uchida, A. Koga, K. Tanaka, and P. Werner, Anomalous temperature dependence of high-harmonic generation in mott insulators, Phys. Rev. Lett. **129**, 157401 (2022).

[54] A. Kofuji and R. Peters, Unconventional gap dependence of high-order harmonic generation in the extremely strong light-matter-coupling regime, Phys. Rev. A **108**, 023521 (2023).

[55] J. Alcalà, U. Bhattacharya, J. Biegert, M. Ciappina, U. Elu, T. Graß, P. T. Grochowski, M. Lewenstein, A. Palau, T. P. H. Sidiropoulos, T. Steinle, and I. Tyulnev, High-harmonic spectroscopy of quantum phase transitions in a high-Tc superconductor, Proc. Natl. Acad. Sci. **119**, e2207766119 (2022).

[56] W. Zhu, B. Fauseweh, A. Chacon, and J.-x. Zhu, Ultrafast laser-driven many-body dynamics and Kondo coherence collapse, Phys. Rev. B **103**, 224305 (2021).

[57] B. Fauseweh and J.-X. Zhu, Laser pulse driven control of charge and spin order in the two-dimensional Kondo lattice, Phys. Rev. B **102**, 165128 (2020).

[58] A. Nakano, K. Uchida, Y. Tomioka, M. Takaya, Y. Okimoto, and K. Tanaka, Dominant role of charge ordering on high harmonic generation in $Pr_{0.6}Ca_{0.4}MnO_3$, arXiv:2309.06537 [Phys. Rev. Res. (to be published)].

[59] C. S. Lange, T. Hansen, and L. B. Madsen, Electron-correlation-induced nonclassicality of light from high-order harmonic generation, Phys. Rev. A **109**, 033110 (2024).

[60] G. P. Zhang, M. S. Si, M. Murakami, Y. H. Bai, and T. F. George, Generating high-order optical and spin harmonics from ferromagnetic monolayers, Nat. Commun. **9**, 3031 (2018).

[61] S. Takayoshi, Y. Murakami, and P. Werner, High-harmonic generation in quantum spin systems, Phys. Rev. B **99**, 184303 (2019).

[62] T. N. Ikeda and M. Sato, High-harmonic generation by electric polarization, spin current, and magnetization, Phys. Rev. B **100**, 214424 (2019).

[63] A. Pattanayak, S. Pujari, and G. Dixit, Role of Majorana fermions in high-harmonic generation from Kitaev chain, Sci. Rep. **12**, 6722 (2022).

[64] M. Kanega, T. N. Ikeda, and M. Sato, Linear and nonlinear optical responses in Kitaev spin liquids, Phys. Rev. Res. **3**, L032024 (2021).

[65] N. M. Allafi, M. H. Kolodrubetz, M. Bukov, V. Oganesyan, and M. Yarmohammadi, Spin high-harmonic generation through terahertz laser-driven phonons, Phys. Rev. B **110**, 064420 (2024).

[66] O. Ly, Noncollinear antiferromagnetic textures driven high-harmonic generation from magnetic dynamics in the absence of spin-orbit coupling, J. Phys.: Condens. Matter **35**, 125802 (2023).

[67] O. Ly and A. Manchon, Spin-orbit coupling induced ultrahigh-harmonic generation from magnetic dynamics, Phys. Rev. B **105**, L180415 (2022).

[68] J. Varela-Manjarres and B. K. Nikolić, High-harmonic generation in spin and charge current pumping at ferromagnetic or antiferromagnetic resonance in the presence of spin–orbit coupling, J. Phys. Mater. **6**, 045001 (2023).

[69] S. Okumura, T. Morimoto, Y. Kato, and Y. Motome, Quadratic optical responses in a chiral magnet, Phys. Rev. B **104**, L180407 (2021).

[70] P. B. Corkum, Plasma perspective on strong field multiphoton ionization, Phys. Rev. Lett. **71**, 1994 (1993).

[71] M. Lewenstein, P. Balcou, M. Y. Ivanov, A. L'Huillier, and P. B. Corkum, Theory of high-harmonic generation by low-frequency laser fields, Phys. Rev. A **49**, 2117 (1994).

[72] G. Vampa, C. R. McDonald, G. Orlando, P. B. Corkum, and T. Brabec, Semiclassical analysis of high harmonic generation in bulk crystals, Phys. Rev. B **91**, 064302 (2015).

[73] A. Nayak, M. Dumergue, S. Kühn, S. Mondal, T. Csizmadia, N. Harshitha, M. Füle, M. Upadhyay Kahaly, B. Farkas, B. Major, V. Szaszkó-Bogár, P. Földi, S. Majorosi, N. Tsatrafyllis, E. Skantzakis, L. Neoričić, M. Shirozhan, G. Vampa, K. Varjú, P. Tzallas *et al.*, Saddle point approaches in strong field physics and generation of attosecond pulses, Phys. Rep. **833**, 1 (2019).

[74] S. Imai, A. Ono, and S. Ishihara, Energy-band echoes: Time-reversed light emission from optically driven quasiparticle wave packets, Phys. Rev. Res. **4**, 043155 (2022).

[75] T. T. Luu, M. Garg, S. Y. Kruchinin, A. Moulet, M. T. Hassan, and E. Goulielmakis, Extreme ultraviolet high-harmonic spectroscopy of solids, Nature (London) **521**, 498 (2015).

[76] G. Vampa, T. J. Hammond, N. Thiré, B. E. Schmidt, F. Légaré, C. R. McDonald, T. Brabec, D. D. Klug, and P. B. Corkum, All-optical reconstruction of crystal band structure, Phys. Rev. Lett. **115**, 193603 (2015).

[77] C. Yu, S. Jiang, T. Wu, G. Yuan, Z. Wang, C. Jin, and R. Lu, Two-dimensional imaging of energy bands from crystal orientation dependent higher-order harmonic spectra in *h*-BN, Phys. Rev. B **98**, 085439 (2018).

[78] L. Li, P. Lan, L. He, W. Cao, Q. Zhang, and P. Lu, Determination of electron band structure using temporal interferometry, Phys. Rev. Lett. **124**, 157403 (2020).

[79] A. J. Uzan-Narovlansky, Á. Jiménez-Galán, G. Orenstein, R. E. F. Silva, T. Arusi-Parpar, S. Shames, B. D. Bruner, B. Yan, O. Smirnova, M. Ivanov, and N. Dudovich, Observation of light-driven band structure via multiband high-harmonic spectroscopy, Nat. Photon. **16**, 428 (2022).

[80] H. Liu, Y. Li, Y. S. You, S. Ghimire, T. F. Heinz, and D. A. Reis, High-harmonic generation from an atomically thin semiconductor, Nat. Phys. **13**, 262 (2017).

[81] C. P. Schmid, L. Weigl, P. Grössing, V. Junk, C. Gorini, S. Schlauderer, S. Ito, M. Meierhofer, N. Hofmann, D. Afanasiev, J. Crewse, K. A. Kokh, O. E. Tereshchenko, J. Güdde, F. Evers, J. Wilhelm, K. Richter, U. Höfer, and R. Huber, Tunable non-integer high-harmonic generation in a topological insulator, Nature (London) **593**, 385 (2021).

[82] Y.-y. Lv, J. Xu, S. Han, C. Zhang, Y. Han, J. Zhou, S.-h. Yao, X.-p. Liu, M.-h. Lu, H. Weng, Z. Xie, Y. B. Chen, J. Hu, Y.-f. Chen, and S. Zhu, High-harmonic generation in Weyl semimetal β-WP$_2$ crystals, Nat. Commun. **12**, 6437 (2021).

[83] T. T. Luu and H. J. Wörner, Measurement of the Berry curvature of solids using high-harmonic spectroscopy, Nat. Commun. **9**, 916 (2018).

[84] Y. Bai, F. Fei, S. Wang, N. Li, X. Li, F. Song, R. Li, Z. Xu, and P. Liu, High-harmonic generation from topological surface states, Nat. Phys. **17**, 311 (2021).

[85] R. E. F. Silva, Á. Jiménez-Galán, B. Amorim, O. Smirnova, and M. Ivanov, Topological strong-field physics on sub-laser-cycle timescale, Nat. Photon. **13**, 849 (2019).

[86] Z. Lou, Y. Zheng, C. Liu, Z. Zeng, R. Li, and Z. Xu, Controlling of the harmonic generation induced by the Berry curvature, Opt. Express **29**, 37809 (2021).

[87] H. B. Banks, Q. Wu, D. C. Valovcin, S. Mack, A. C. Gossard, L. Pfeiffer, R.-B. Liu, and M. S. Sherwin, Dynamical birefringence: Electron-hole recollisions as probes of berry curvature, Phys. Rev. X **7**, 041042 (2017).

[88] L. Yue and M. B. Gaarde, Characterizing anomalous high-harmonic generation in solids, Phys. Rev. Lett. **130**, 166903 (2023).

[89] A. J. Uzan-Narovlansky, L. Faeyrman, G. G. Brown, S. Shames, V. Narovlansky, J. Xiao, T. Arusi-Parpar, O. Kneller, B. D. Bruner, O. Smirnova, R. E. F. Silva, B. Yan, Á. Jiménez-Galán, M. Ivanov, and N. Dudovich, Observation of interband Berry phase in laser-driven crystals, Nature (London) **626**, 66 (2024).

[90] L. Wu, S. Patankar, T. Morimoto, N. L. Nair, E. Thewalt, A. Little, J. G. Analytis, J. E. Moore, and J. Orenstein, Giant anisotropic nonlinear optical response in transition metal monopnictide Weyl semimetals, Nat. Phys. **13**, 350 (2017).

[91] L. Medic, J. Mravlje, A. Ramšak, and T. Rejec, High-harmonic generation in semi-Dirac and Weyl semimetals with broken time-reversal symmetry: Exploration of the merging of Weyl nodes, Phys. Rev. B **109**, 205130 (2024).

[92] N. Nagaosa and Y. Tokura, Topological properties and dynamics of magnetic skyrmions, Nat. Nanotechnol. **8**, 899 (2013).

[93] Y. Hayashi, Y. Okamura, N. Kanazawa, T. Yu, T. Koretsune, R. Arita, A. Tsukazaki, M. Ichikawa, M. Kawasaki, Y. Tokura, and Y. Takahashi, Magneto-optical spectroscopy on Weyl nodes for anomalous and topological Hall effects in chiral MnGe, Nat. Commun. **12**, 5974 (2021).

[94] S. Sorn, L. Yang, and A. Paramekanti, Resonant optical topological Hall conductivity from skyrmions, Phys. Rev. B **104**, 134419 (2021).

[95] W. Feng, J.-p. Hanke, X. Zhou, G.-y. Guo, S. Blügel, Y. Mokrousov, and Y. Yao, Topological magneto-optical effects and their quantization in noncoplanar antiferromagnets, Nat. Commun. **11**, 118 (2020).

[96] Y. D. Kato, Y. Okamura, M. Hirschberger, Y. Tokura, and Y. Takahashi, Topological magneto-optical effect from skyrmion lattice, Nat. Commun. **14**, 5416 (2023).

[97] X. Li, C. Liu, Y. Zhang, S. Zhang, H. Zhang, Y. Zhang, W. Meng, D. Hou, T. Li, C. Kang, F. Huang, R. Cao, D. Hou, P. Cui, W. Zhang, T. Min, Q. Lu, X. Xu, Z. Sheng, B. Xiang, and Z. Zhang, Topological Kerr effects in two-dimensional magnets with broken inversion symmetry, Nat. Phys. **20**, 1145 (2024).

[98] V. D. Esin, A. A. Avakyants, A. V. Timonina, N. N. Kolesnikov, and E. V. Deviatov, Second-harmonic response in magnetic nodal-line semimetal Fe$_3$GeTe$_2$, Chinese Phys. Lett. **39**, 097303 (2022).

[99] T. Hori, N. Kanazawa, K. Matsuura, H. Ishizuka, K. Fujiwara, A. Tsukazaki, M. Ichikawa, M. Kawasaki, F. Kagawa, M. Hirayama, and Y. Tokura, Strongly pinned skyrmionic bubbles and higher-order nonlinear Hall resistances at the interface of Pt/FeSi bilayer, Phys. Rev. Mater. **8**, 044407 (2024).

[100] I. Martin and C. D. Batista, Itinerant electron-driven chiral magnetic ordering and spontaneous quantum hall effect in triangular lattice models, Phys. Rev. Lett. **101**, 156402 (2008).

[101] Y. Akagi and Y. Motome, Spin chirality ordering and anomalous hall effect in the ferromagnetic kondo lattice model on a triangular lattice, J. Phys. Soc. Jpn. **79**, 083711 (2010).

[102] H. Takagi, R. Takagi, S. Minami, T. Nomoto, K. Ohishi, M.-T. Suzuki, Y. Yanagi, M. Hirayama, N. D. Khanh, K. Karube, H. Saito, D. Hashizume, R. Kiyanagi, Y. Tokura, R. Arita, T. Nakajima, and S. Seki, Spontaneous topological Hall effect induced by non-coplanar antiferromagnetic order in intercalated van der Waals materials, Nat. Phys. **19**, 961 (2023).

[103] P. Park, W. Cho, C. Kim, Y. An, Y.-g. Kang, M. Avdeev, R. Sibille, K. Iida, R. Kajimoto, K. H. Lee, W. Ju, E.-J. Cho, H.-J. Noh, M. J. Han, S.-S. Zhang, C. D. Batista, and J.-G. Park, Tetrahedral triple-Q magnetic ordering and large spontaneous Hall conductivity in the metallic triangular antiferromagnet $Co_{1/3}TaS_2$, Nat. Commun. **14**, 8346 (2023).

[104] P. Park, W. Cho, C. Kim, Y. An, M. Avdeev, K. Iida, R. Kajimoto, and J.-G. Park, Composition dependence of bulk properties in the Co-intercalated transition metal dichalcogenide $Co_{1/3}TaS_2$, Phys. Rev. B **109**, L060403 (2024).

[105] A. Ono and Y. Akagi, Photocontrol of spin scalar chirality in centrosymmetric itinerant magnets, Phys. Rev. B **108**, L100407 (2023).

[106] S. Maekawa, T. Tohyama, S. E. Barnes, S. Ishihara, W. Koshibae, and G. Khaliullin, *Physics of Transition Metal Oxides* (Springer, Berlin, 2004).

[107] In a minimal ferromagnetic Kondo lattice model defined in Eq. (1) only with the nearest neighbor transfer integral, the scalar chiral state is not stable at $n_e = 0.5$ [101]. Nevertheless, we can stabilize the scalar chiral state by introducing superexchange interactions [101,120,121] or Dzyaloshinskii–Moriya interactions between localized spins, although such magnetic interactions do not directly affect the electronic structure. Since we are currently interested in HHG in the presence of topological spin textures, we do not delve into the mechanisms stabilizing the scalar chiral state [122], and instead, we fix the localized spins to analyze the real-time evolution of electrons.

[108] As shown in Fig. 6, the power spectrum also differs with the chirality sign for other polarization angles.

[109] S. Kitamura, N. Nagaosa, and T. Morimoto, Nonreciprocal Landau–Zener tunneling, Commun. Phys. **3**, 63 (2020).

[110] S. Takayoshi, J. Wu, and T. Oka, Nonadiabatic nonlinear optics and quantum geometry — Application to the twisted Schwinger effect, SciPost Phys. **11**, 075 (2021).

[111] A. Ono and S. Ishihara, Double-exchange interaction in optically induced nonequilibrium state: A conversion from ferromagnetic to antiferromagnetic structure, Phys. Rev. Lett. **119**, 207202 (2017).

[112] A. Ono and S. Ishihara, Photocontrol of magnetic structure in an itinerant magnet, Phys. Rev. B **98**, 214408 (2018).

[113] K. Hattori, H. Watanabe, J. Iguchi, T. Nomoto, and R. Arita, Effect of collective spin excitations on electronic transport in topological spin textures, Phys. Rev. B **110**, 014425 (2024).

[114] O. E. Alon, V. Averbukh, and N. Moiseyev, Selection rules for the high harmonic generation spectra, Phys. Rev. Lett. **80**, 3743 (1998).

[115] X. Liu, X. Zhu, L. Li, Y. Li, Q. Zhang, P. Lan, and P. Lu, Selection rules of high-order-harmonic generation: Symmetries of molecules and laser fields, Phys. Rev. A **94**, 033410 (2016).

[116] O. Neufeld, D. Podolsky, and O. Cohen, Floquet group theory and its application to selection rules in harmonic generation, Nat. Commun. **10**, 405 (2019).

[117] T. N. Ikeda, High-order nonlinear optical response of a twisted bilayer graphene, Phys. Rev. Res. **2**, 032015(R) (2020).

[118] M. Kanega and M. Sato, High-harmonic generation in graphene under the application of a DC electric current: From perturbative to nonperturbative regime, Phys. Rev. B **110**, 035303 (2024).

[119] M.-T. Suzuki, T. Koretsune, M. Ochi, and R. Arita, Cluster multipole theory for anomalous Hall effect in antiferromagnets, Phys. Rev. B **95**, 094406 (2017).

[120] Y. Akagi and Y. Motome, Noncoplanar spin canting in lightly-doped ferromagnetic Kondo lattice model on a triangular lattice, J. Phys.: Conf. Ser. **320**, 012059 (2011).

[121] Y. Akagi and Y. Motome, Spontaneous formation of kagome network and Dirac half-semimetal on a triangular lattice, Phys. Rev. B **91**, 155132 (2015).

[122] Y. Akagi, M. Udagawa, and Y. Motome, Hidden multiple-spin interactions as an origin of spin scalar chiral order in frustrated kondo lattice models, Phys. Rev. Lett. **108**, 096401 (2012).